ACADEMIC PRESS

Available online at www.sciencedirect.com

SCIENCE DIRECT®

Journal of Sound and Vibration 268 (2003) 429–463

JOURNAL OF SOUND AND VIBRATION

www.elsevier.com/locate/jsvi

A spectral finite element for analysis of wave propagation in uniform composite tubes

D. Roy Mahapatra, S. Gopalakrishnan*

Department of Aerospace Engineering, Indian Institute of Science, Bangalore 560012, India

Received 14 February 2002; accepted 20 November 2002

Abstract

A spectral finite element model (SFEM) for analysis of coupled broadband wave propagation in composite tubular structure is presented. Wave motions in terms of three translational and three rotational degrees of freedom at tube cross-section are considered based on first order shear flexible cylindrical bending, torsion and secondary warping. Solutions are obtained in wavenumber space by solving the coupled wave equation in 3-D. An efficient and fully automated computational strategy is developed to obtain the wavenumbers of coupled wave modes, spectral element shape function, strain–displacement matrix and the exact dynamic stiffness matrix. The formulation emphasizes on a compact matrix methodology to handle large-scale computational model of built-up network of such cylindrical waveguides. Thickness and frequency limits for application of the element is discussed. Performance of the element is compared with analytical solution based on membrane shell kinematics. A map of the distribution of vibrational modes in wavelength and time scales is presented. Effect of fiber angle on natural frequencies, phase and group dispersions are also discussed. Numerical simulations show the ease with which dynamic responses can be obtained efficiently. Parametric studies on a clamped–free graphite–epoxy composite tube under short-impulse load are carried out to obtain the effect of various composite configurations and tube geometries on the response.
© 2003 Elsevier Science Ltd. All rights reserved.

1. Introduction

Metallic tubular structures are used extensively in piping and skeletal components. There are increasing usage of fiber-wound and laminated composite cylinders and tubes in automobiles, aircrafts and spacecrafts. For their high strength, high stiffness and light weight, graphite–epoxy composite strut tubes have been chosen for International Space Station (ISS) Freedom [1]. Due to

*Corresponding author. Tel.: +91-80-309-2757; fax: +91-80-360-0134.
E-mail address: krishnan@aero.iisc.ernet.in (S. Gopalakrishnan).

0022-460X/03/$ - see front matter © 2003 Elsevier Science Ltd. All rights reserved.
doi:10.1016/S0022-460X(02)01539-0

high-load carrying ability under pressurized condition, such tubular beams are useful in inflatable space structures [2]. Significant research has been reported in literature to address issues related to vibration and noise transmission [3], impact dynamics, fatigue and damage in such structural components. In problems related to high-frequency vibration, noise transmission and impact, many analytical and numerical methods based on wave motion have been reported. The present work deals with development of a new spectral finite element (FE) for efficient analysis of broadband wave propagation in uniform composite tubes and connected skeletal structures. Also, special emphasis is made to model coupled wave propagation in such uniform tubular element due to variation in the angle of laminated composite ply orientation and fiber winding.

Composite tubular structures can be modelled in two ways: (1) The general method is to use cylindrical shell kinematics. Various theories (e.g., by Mirsky and Hermann [4], Cooper and Naghdi [5], Greenspon [6], and later by Reddy and Liu [7], Leissa and Chang [8] and Qatu [9] for composite shell) in this direction have been reported, which are based on the simpler and computationally tractable framework and observations of infinite order frequency spectral characteristics from three-dimensional (3-D) analysis [10]. Xi et al. [11] has used 3-D elasticity solution and shell radial displacement from finite strip element analysis to develop semi-analytical model to study of characteristic waves, their phase and group dispersions in laminated composite cylindrical shell. (2) For closed cylindrical shell, often it is useful to represent an equivalent thin-walled beam kinematics and this latter approximation based on non-axially symmetric first order shear kinematics is used in the present work.

For uniform circular cylinders, singly curved shell kinematics is sufficient. For coupled wave propagation analysis, the displacement field in this case requires in-plane displacements, bi-directional bending and rotation about the shell normal. For a thick shell, transverse shear deformation becomes significant and 30% or higher error in deflection and natural frequencies may occur when the effect of such shear is neglected [12]. Considering first order shear deformation in laminated anisotropic shells, FE results and exact results for simply supported boundary conditions have been reported in the work of Reddy [13,14], Chandrashekhara [15] and Sun et al. [12]. In high-frequency vibration analysis, it is essential to consider the wave band, and representation of the entire modal group is important compared to accuracy of one or two specific vibration modes. Therefore, analysis in wavenumber space (k space) is found most suitable. Langley [16,17] has studied modal density and energy flow in cylindrical shells using semi-numerical analysis. Smith [18] has discussed various types of wave propagation in closed cylinders. Fuller and Fahy [19] have discussed propagation of axial waves in fluid-filled cylindrical shell. Recently, frequency-domain methods have been developed by Xi et al. [20], and Ruzzene and Baz [21] for analysis of longitudinal and circumferential wave motion in fluid-loaded cylindrical shells. The strip element method developed in Ref. [20] has also been used for studying the complex wave-mode coupling due to anisotropy and finite shell thickness in laminated composite [11] and functionally graded cylinders [22,23]. As pointed out in Refs. [3] and [17], the wave amplitudes for in-plane and flexural (circumferential) motions have significant scale difference. However, Bennet and Accorsi [24] have shown that in the presence of ring stiffeners, wave energy flow has stop bands, which are broadband and can be tuned to required frequency band. It can be seen from the expression of ring frequency [17] given by $\omega_R = (1/R)\sqrt{E/\rho(1-\nu^2)}$ (for flexural wave motion in cylindrical isotropic shell) that natural frequency increases as the radius of curvature R decreases. This tells us that for closed circular cylinders with shorter span

and higher thickness-to-radius ratio, the flexural vibrational modes take transition from low- to high-frequency zone and fall in comparable scale with in-plane motion. In addition, the rotation about the shell normal causes overall torsional motion in such tubular structure and interacts with the in-plane and flexural motion depending upon the geometrical parameter $\eta = h/R$, where $2h$ is the shell thickness. This length–scale interaction has significance for coupled wave propagation in laminated or fiber-wound composite tubular structures due to wide scope of tailorability. Further, for broadband wave propagation (waves with low as well as high group speeds for axial, flexural and torsional motion in composite tube), a time scale $\tau = Rc_g^{-1}$ characterizes the dynamics, where $c_g(= \mathrm{d}\omega/\mathrm{d}k)$ is the group speed of a particular type of wave. Kaplunov et al. [25] have discussed the wave motion in thin-walled elastic bodies considering the above scale effects.

Several studies on free and forced vibration of composite thin-walled bodies have been reported. Song and Liberescu [26] have modelled composite thin-walled closed-section beams considering non-classical effects such as primary and secondary warping. Rand [27] has carried out closed-form analysis of thin-walled beams with arbitrary cross-sections and out-of-plane warping under static loading. Effect of bending-twist coupling and extension-bending coupling for different lamination angles have been investigated in the above work. Influence of similar coupling effects on free vibration response of anisotropic thin-walled closed-section beams have been reported by Armanios and Badir [28] and Dancila and Armanios [29]. Ferrero et al. [30] have studied uncoupled torsional motion in thin-walled composite beams with mid-plane symmetry. In the present paper, we consider coupling between axial, flexural and torstional wave modes in first order shear deformable composite tube in a general form and present computational strategy to deal with broadband wave propagation.

Although there are many important applications of high-frequency vibration and elastic wave propagation in composite thin-walled structures in rotorcrafts, turbomachinery, piping and skeletal structures, efficient and automated modelling strategies and computational simulations needs further development. In most of these cases, attempts to solve the problems in closed form become enormously complex. On the other hand, while using standard FE methods, much care is needed to ensure appropriate mesh and solution scheme using large number of cylindrical shell elements or thin-walled beam elements to capture higher order vibrational modes. Wang et al. [31] have developed theoretical solution for orthotropic thick cylindrical shell under impact load based on finite Hankel transform and Laplace transform and validated the results using axisymmetric FE model. Frequency-domain-based spectral analysis of wave motion in thin-walled bodies has been discussed by Doyle [32]. Also, structural acoustics of a complete cylindrical cavity has been studied here by solving Helmholtz equation in cylindrical co-ordinate. Spectral FEs for coupled wave propagation in laminated composite beams and related practical issues have been reported in earlier works of the authors [33,34].

In the present paper, a new FE is developed for uniform circular composite tube with general fiber orientation. This FE model uses fast Fourier transform (FFT) to uncouple space and time from the 3-D coupled wave equations and boundary equations. The set of ordinary differential equations (ODEs) thus obtained are used in Fourier domain to construct the FE model and system assembly. Apart from handling the coupled wave modes, this model called spectral finite element model (SFEM) has the following advantages: (1) It allows one to use a single element to represent an uniform tube in a connected structure due to exact inertial distribution. (2) Under any transient loading, frequency as well as time responses can be post-processed easily using

forward and inverse FFT, which has been integrated with a general purpose code. (3) For a single uniform tube, the system size is 12×12 and broadband wave propagation analysis in large network of such structures can be performed with many order smaller system size and lesser computation time compared to standard FE models and (4) frequency response function (transfer function) is the by-product of the approach.

2. Linear wave motion in composite tube

Considering the reference X-axis of the cylinder (Fig. 1) passing through the center of the annular cross-section, the displacement field can be written in terms of three primary displacements u^o, v^o and w^o and three cross-sectional rotations θ_x, θ_y and θ_z at the center as follows:

$$u(x,y,z,t) = u^o(x,t) + z\left[1 + \frac{\xi}{\sqrt{y^2+z^2}}\right]\theta_y(x,t) + y\left[1 - \frac{\xi}{\sqrt{y^2+z^2}}\right]\theta_z(x,t), \tag{1}$$

$$v(x,y,z,t) = v^o(x,t) - z\theta_x(x,t), \tag{2}$$

$$w(x,y,z,t) = w^o(x,t) + y\theta_x(x,t). \tag{3}$$

where u, v and w are the longitudinal, lateral and transverse displacements, respectively at a material point (x,y,z). θ_x, θ_y and θ_z are the torsional, transverse bending and lateral bending rotations. ξ is the normal distance of a material point measured from the mid-plane reference contour. We assume that any straight line representing the mean diameter of a circular lay-up remains straight during deformation. This leads to first order shear flexibility of the annular cross-section. Such shear flexibility can be considered when appropriate shear correction factor is introduced and will be discussed later. Note that primary warping for a circular contour is zero and only secondary warping can occur, which can be derived from the formulations given by Song and Liberescu [26]. As seen in the expression of axial displacement field ($u(x,y,z,t)$) in Eq. (1), the non-linear terms appear as the combined effect of bending and radial displacement (circumferential mode) of the reference contour and is termed as ovaling. Also note that in the

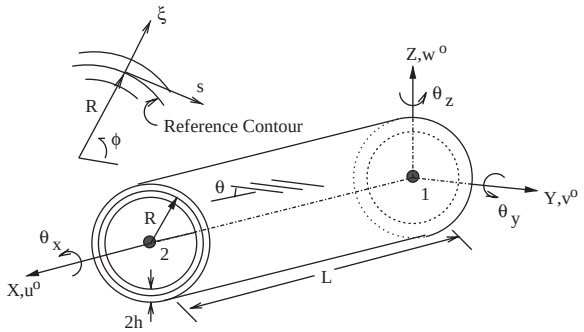

Fig. 1. Co-ordinate system and d.o.f.'s for the spectral FE for uniform composite tube. Two FE nodes are shown with solid circles.

above higher order cylindrical bending model, displacement continuity at the mid-plane contour is ensured. The bending rotations θ_y and θ_z are independent of the curvature and assumed constant throughout the cross-section as in case of Timoshenko beam model. Further details regarding similar higher order models for thin-walled closed section beams can be found in Refs. [26,28]. The global bending mode has multiplicity of two due to cross-sectional symmetry about Y- and Z-axis. The circumferential modes consist of antisymmetric and symmetric thickness stretching. Resonant wavenumbers for the antisymmetric thickness stretching of a complete circular cylindrical shell simply supported at the ends is $k = 2m\pi/S$, S being the arc length, has been discussed by Langley [17]. The symmetric thickness stretching is a local higher order effect due to the Poisson ratio and is of significance only for large $\eta = h/R$ and is beyond the scope of the present thin-walled-beam-type modelling. For uncoupled flexural motion of the cylindrical shell surface, the associated natural frequency is same as the ring frequency (discussed in the introduction).

In the following and subsequent derivations, small letters with bold face are used to represent vectors and capital letters with bold face are used to represent matrices. The constitutive relation in the element co-ordinate system (X, Y, Z) is first expressed as

$$\begin{Bmatrix} \sigma_{xx} \\ \tau_{xz} \\ \tau_{xy} \end{Bmatrix} = \bar{\bar{\mathbf{Q}}} \begin{Bmatrix} \varepsilon_{xx} \\ \gamma_{xz} \\ \gamma_{xy} \end{Bmatrix}, \tag{4}$$

where

$$\bar{\bar{\mathbf{Q}}} = \begin{bmatrix} 1 & 0 & 0 \\ 0 & \sin\phi & \cos\phi \\ 0 & \cos\phi & -\sin\phi \end{bmatrix} \begin{bmatrix} \bar{Q}_{11} & 0 & \bar{Q}_{16} \\ 0 & \bar{Q}_{55} & 0 \\ \bar{Q}_{16} & 0 & \bar{Q}_{66} \end{bmatrix} \begin{bmatrix} 1 & 0 & 0 \\ 0 & \sin\phi & \cos\phi \\ 0 & \cos\phi & -\sin\phi \end{bmatrix}. \tag{5}$$

ϕ is the polar angle of a material point in the cross-sectional plane YZ (shown in Fig. 1). Expression for the elements of the matrix $\bar{\mathbf{Q}}$ are obtained from the elasticity matrix $\mathbf{C}$ (given in Ref. [35]) for transversely orthotropic plies in fiber-local co-ordinate system, then by rotating in the ply-local system (x, s, ξ) and then imposing plane-stress condition on the thin-walled surface (radius of curvature R) as $\sigma_{\xi\xi} = 0$, $\tau_{s\xi} = 0$ and $\tau_{x\xi} = 0$ as discussed in Ref. [27]. This gives rise to the matrix $\bar{\mathbf{Q}}$, whose elements can be expressed as

$$\bar{Q}_{11} = Q_{11} - \frac{1}{\Delta} Q_{12}(Q_{13}Q_{23} - Q_{33}Q_{12}) + \frac{1}{\Delta} Q_{13}(Q_{22}Q_{13} - Q_{12}Q_{23}), \tag{6}$$

$$\bar{Q}_{16} = Q_{16} + \frac{1}{\Delta} Q_{26}(Q_{12}Q_{33} - Q_{13}Q_{23}), \quad \bar{Q}_{55} = Q_{55} - \frac{Q_{45}^2}{Q_{44}}, \tag{7}$$

$$\bar{Q}_{66} = Q_{66} + \frac{1}{\Delta} Q_{26}(Q_{26}Q_{33} - Q_{23}Q_{36}), \quad \Delta = Q_{23}^2 - Q_{33}Q_{22}, \tag{8}$$

and

$$\mathbf{Q} = \Gamma^{\mathrm{T}} \mathbf{C} \Gamma, \tag{9}$$

is the transformation of the elasticity matrix $\mathbf{C}$ from the fiber-local co-ordinates to the ply-local co-ordinates, where θ (shown in Fig. 1) represents the fiber orientation in the ply-local co-ordinate system.

Shear moduli $\bar{Q}_{44}, \bar{Q}_{55}$ and $\bar{Q}_{66}$ are multiplied by a shear correction factor (K'), which can be computed from the expression proposed by Cowper [36] as

$$K' = \frac{6(1+\nu)(1+h'^2)^2}{(7+6\nu)(1+h'^2)^2 + (20+12\nu)h'^2}, \quad h' = \frac{R-h}{R+h}, \tag{10}$$

where $\nu = \nu_{23}, \nu_{13}$ and ν_{12} corresponding to $\bar{Q}_{44}, \bar{Q}_{55}$ and $\bar{Q}_{66}$, respectively. In the process of deriving the governing equations of motion and force boundary equations, we come across many higher order stiffness and mass coefficients, which in compact notation, are expressed, respectively, as

$$\mathbf{A}_{jl} = \int_0^{2\pi} \int_{R-h}^{R+h} \bar{\bar{Q}}_{jl} \Psi^{\mathrm{T}} \Psi \, r \, \mathrm{d}r \, \mathrm{d}\phi, \quad \mathbf{M} = \int_0^{2\pi} \int_{R-h}^{R+h} \rho \Psi^{\mathrm{T}} \Psi \, r \, \mathrm{d}r \, \mathrm{d}\phi, \tag{11}$$

where

$$\Psi = \{1 \;\; y \;\; z \;\; \bar{y} \;\; \bar{z} \;\; \bar{y},_y \;\; \bar{y},_z \;\; \bar{z},_y \;\; \bar{z},_z \}, \tag{12}$$

$$\bar{y} = yR(y^2+z^2)^{-1/2}, \quad \bar{z} = z\{2 - R(y^2+z^2)^{-1/2}\}, \tag{13}$$

$$y = r\cos\phi, \quad z = r\sin\phi, \quad r = R + \xi. \tag{14}$$

Note that in Eq. (11), $\mathbf{A}_{jl}$ is a 9×9 matrix for each of $\bar{\bar{Q}}_{jl}$, and hence we shall use additional two subscripts after jl while expressing a single stiffness coefficient in the following derivations. The explicit forms of $\mathbf{A}_{jl}$ and $\mathbf{M}$ are given in the appendix. Now, the six wave equations derived using Hamilton's principle pertaining to six primary displacement variables can be arranged as follows:

$$\begin{aligned}\delta u^o : 0 = {} & M_{11}\ddot{u}^o + M_{15}\ddot{\theta}_y + M_{14}\ddot{\theta}_z - A_{1111}u^o_{,xx} - A_{1611}v^o_{,xx} - A_{1511}w^o{}_{,xx} \\ & - (A_{1512} - A_{1613})\theta_x{}_{,xx} - A_{1115}\theta_y{}_{,xx} - A_{1114}\theta_z{}_{,xx} - (A_{1519} + A_{1618})\theta_y{}_{,x} \\ & - (A_{1517} + A_{1616})\theta_z{}_{,x}\,,\end{aligned} \tag{15}$$

$$\begin{aligned}\delta v^o : 0 = {} & M_{11}\ddot{v}^o - M_{13}\ddot{\theta}_x - A_{1611}u^o_{,xx} - A_{6611}v^o_{,xx} - A_{5611}w^o_{,xx} \\ & - (A_{5612} - A_{6613})\theta_x{}_{,xx} - A_{1615}\theta_y{}_{,xx} - A_{1614}\theta_z{}_{,xx} - (A_{5619} + A_{6618})\theta_y{}_{,x} \\ & - (A_{5617} + A_{6616})\theta_z{}_{,x}\,,\end{aligned} \tag{16}$$

$$\begin{aligned}\delta w^o : 0 = {} & M_{11}\ddot{w}^o + M_{12}\ddot{\theta}_x - A_{1511}u^o_{,xx} - A_{5611}v^o_{,xx} - A_{5511}w^o_{,xx} \\ & - (A_{5512} - A_{5613})\theta_x{}_{,xx} - A_{1515}\theta_y{}_{,xx} - A_{1514}\theta_z{}_{,xx} - (A_{5519} + A_{5618})\theta_y{}_{,x} \\ & - (A_{5517} + A_{5616})\theta_z{}_{,x}\,,\end{aligned} \tag{17}$$

$$\begin{aligned}\delta\theta_x : 0 = {} & (M_{22}+M_{33})\ddot{\theta}_x - M_{13}\ddot{v}^o + M_{12}\ddot{w}^o - (A_{1512}-A_{1613})u^o_{,xx} \\ & - (A_{5612}-A_{6613})v^o_{,xx} - (A_{5512}-A_{5613})w^o_{,xx} \\ & - (A_{5522}-2A_{5623}+A_{6633})\theta_{x,xx} \\ & - (A_{1525}-A_{1635})\theta_{y,xx} - (A_{1524}-A_{1634})\theta_{z,xx} \\ & - (A_{5529}+A_{5628}-A_{5639}-A_{6638})\theta_{y,x} \\ & - (A_{5527}+A_{5626}\,A_{5637}-A_{6636})\theta_{z,x}\,, \end{aligned} \tag{18}$$

$$\begin{aligned}\delta\theta_y : 0 = {} & M_{55}\ddot{\theta}_y + M_{15}\ddot{u}^o + M_{45}\ddot{\theta}_z - A_{1115}u^o_{,xx} - A_{1615}v^o_{,xx} - A_{1515}w^o_{,xx} \\ & - (A_{1525}-A_{1635})\theta_{x,xx} - A_{1155}\theta_{y,xx} - A_{1145}\theta_{z,xx} \\ & + (A_{1519}+A_{1618})u^o_{,x} + (A_{5619}+A_{6618})v^o_{,x} + (A_{5519}+A_{5618})w^o_{,x} \\ & + (A_{5529}+A_{5628}-A_{5639}-A_{6638})\theta_{x,x} + (A_{1648}+A_{1549}-A_{1557} \\ & - A_{1656})\theta_{z,x} + (A_{5599}+2A_{5689}+A_{6688})\theta_y \\ & + (A_{5579}\,A_{5669}+A_{5678}+A_{6668})\theta_z, \end{aligned} \tag{19}$$

$$\begin{aligned}\delta\theta_z : 0 = {} & M_{44}\ddot{\theta}_z + M_{14}\ddot{u}^o + M_{45}\ddot{\theta}_y - A_{1114}u^o_{,xx} - A_{1614}v^o_{,xx} - A_{1514}w^o_{,xx} \\ & - (A_{1524}-A_{1634})\theta_{x,xx} - A_{1145}\theta_{y,xx} - A_{1144}\theta_{z,xx} \\ & + (A_{1517}+A_{1616})u^o_{,x} + (A_{5617}+A_{6616})v^o_{,x} + (A_{5517}+A_{5616})w^o_{,x} \\ & + (A_{5527}+A_{5626}-A_{5637}-A_{6636})\theta_{x,x} + (A_{1557}+A_{1656}-A_{1549} \\ & - A_{1648})\theta_{y,x} + (A_{5579}+A_{5678}+A_{5669}+A_{6668})\theta_y \\ & + (A_{5577}+2A_{5667}+A_{6666})\theta_z, \end{aligned} \tag{20}$$

and the associated force boundary equations can be obtained as

$$\begin{aligned} & A_{1111}u^o_{,x} + A_{1611}v^o_{,x} + A_{1511}w^o_{,x} + (A_{1512}-A_{1613})\theta_{x,x} + A_{1115}\theta_{y,x} + A_{1114}\theta_{z,x} \\ & + (A_{1519}+A_{1618})\theta_y + (A_{1517}+A_{1616})\theta_z = N_x, \end{aligned} \tag{21}$$

$$\begin{aligned} & A_{1611}u^o_{,x} + A_{6611}v^o_{,x} + A_{5611}w^o_{,x} + (A_{5612}-A_{6613})\theta_{x,x} + A_{1615}\theta_{y,x} + A_{1614}\theta_{z,x} \\ & + (A_{5619}+A_{6618})\theta_y + (A_{5617}+A_{6616})\theta_z = V_{xy}, \end{aligned} \tag{22}$$

$$\begin{aligned} & A_{1511}u^o_{,x} + A_{5611}v^o_{,x} + A_{5511}w^o_{,x} + (A_{5512}-A_{5613})\theta_{x,x} + A_{1515}\theta_{y,x} + A_{1514}\theta_{z,x} \\ & + (A_{5519}+A_{5618})\theta_y + (A_{5517}+A_{5616})\theta_z = V_{xz}, \end{aligned} \tag{23}$$

$$\begin{aligned} & (A_{1512}-A_{1613})u^o_{,x} + (A_{5612}-A_{6613})v^o_{,x} + (A_{5512}-A_{5613})w^o_{,x} + (A_{5522} \\ & - 2A_{5623}+A_{6633})\theta_{x,x} + (A_{1525}-A_{1635})\theta_{y,x} + (A_{1524}-A_{1634})\theta_{z,x} + (A_{5529} \\ & + A_{5628}-A_{5639}-A_{6638})\theta_y + (A_{5527}+A_{5626}-A_{5637}-A_{6636})\theta_z = M_x, \end{aligned} \tag{24}$$

$$\begin{aligned} & A_{1115}u^o_{,x} + A_{1615}v^o_{,x} + A_{1515}w^o_{,x}(A_{1525}-A_{1635})\theta_{x,x} + A_{1155}\theta_{y,x} + A_{1145}\theta_{z,x} \\ & + (A_{1559}+A_{1658})\theta_y + (A_{1557}+A_{1656})\theta_z = M_y, \end{aligned} \tag{25}$$

$$A_{1114}u^o_{,x} + A_{1614}v^o_{,x} + A_{1514}w^o_{,x} + (A_{1524} - A_{1634})\theta_{x,x} + A_{1145}\theta_{y,x} + A_{1144}\theta_{z,x} + (A_{1549} + A_{1648})\theta_y + (A_{1547} + A_{1646})\theta_z = M_z. \tag{26}$$

Here, $\langle . \rangle_{,x}$ represents derivative with respect to x. We solve the wave equations (15)–(20) exactly in frequency domain. However, the numerical procedure involves some iterative approximations due to unavailability of the closed-form solution to the wavenumbers. This issue is discussed in detail at the end of this section. The wave type solution thus obtained is finally used to construct the Fourier domain shape function for semi-infinite and finite tube element. Here, the meaning of spectral element shape function at a particular frequency (sampling frequency in discrete Fourier transform (DFT)) is similar to the pseudo-static shape function in time-domain FE at a particular time step. This concept encompasses the basic framework for the development of SFEM and has been implemented in the earlier works [33,34]. To proceed further, we consider asymptotic solution to the primary field vector given by

$$\mathbf{u}(x,t) = \sum_{n=1}^{N} \hat{\mathbf{u}}(x,\omega_n)\, \mathrm{e}^{\mathrm{i}\omega_n t}, \tag{27}$$

where $\hat{(\cdot)}$ represents the spectral amplitude. $\hat{\mathbf{u}}(x,\omega_n) = \{\hat{u}^o\ \hat{v}^o\ \hat{w}^o\ \hat{\theta}_x\ \hat{\theta}_y\ \hat{\theta}_z\}^{\mathrm{T}}$ represents the generic displacement vector along the reference X-axis of the tube element and $\mathrm{i} = \sqrt{-1}$. ω_n is the structural frequency at FFT sampling points and N is the Nyquist point in FFT. In the following discussions, displacements, strains, stresses, forces, etc. will mean their spectral amplitude unless explicitly written otherwise. After decoupling, the time harmonic component $\mathrm{e}^{\mathrm{i}\omega_n t}$ from the spatial component in Eq. (27), the spectral amplitudes can be expressed as sum of all the wave modes in the form $\mathrm{e}^{-\mathrm{i}k_j x}$ [32], where k_j is the wavenumber associated with jth wave mode. Thus, spatial variation in terms of wavenumbers can be expressed as

$$\hat{\mathbf{u}}(x,\omega_n) = \mathbf{R}\Lambda_0\tilde{\mathbf{u}} = \mathbf{T}_1(x,\omega_n)\tilde{\mathbf{u}}, \tag{28}$$

where $\tilde{\mathbf{u}}$ represents the wave coefficient vector. $\Lambda_{0(12\times12)}$ is a diagonal matrix with asymptotic entries in characteristic wavenumbers ($k_j, j = 1, \ldots, 12$) and can be expressed as

$$\Lambda_{0jj} = \begin{cases} \mathrm{e}^{-\mathrm{i}k_j x} & \text{if } k_j \text{ is } +\text{ve real}, \\ \mathrm{e}^{+\mathrm{i}k_j (L-x)} & \text{if } k_j \text{ is } -\text{ve real}, \\ \mathrm{e}^{+\mathrm{i}k_j (L-x)} & \text{if } k_j \text{ is } +\text{ve imaginary}, \\ \mathrm{e}^{-\mathrm{i}k_j x} & \text{if } k_j \text{ is } -\text{ve imaginary}. \end{cases} \tag{29}$$

Classification of the exponential entries in Eq. (29) is to keep track of propagating and evanescent wave components at each FFT sampling frequencies. In Eq. (28), $\mathbf{R}_{(6\times12)}$ is defined as the amplitude ratio matrix and is associated with the wave coefficient vector. This is explained in the next section. Each of k_j in Eq. (29) are obtained as root of the 12th order characteristic equation (also called dispersion equation):

$$\mathrm{Det}\,\mathbf{F}(k_j) = 0, \tag{30}$$

obtained by substituting Eqs. (27) and (28) in the wave equations. Here, $\mathbf{F}(k_j)$ is a 6×6 complex matrix. Although the mathematical representation is exact one, the wavenumbers are computed numerically as mentioned earlier at each FFT sampling frequency over the broad-frequency

window. However, for a fully coupled composite configuration arising from thickness-wise asymmetric fiber winding or lay-up, correlating a particular root to its mode of propagation is not straight-forward as seen in the complexity in Eqs. (15)–(20). Due to this, significant numerical error may occur, especially at frequency bands where phase-dispersion cross-overs among different modes appear. In this work, we adopt a k subspace averaging scheme to speed up computation with improved accuracy. This involves computation of wavenumbers as in the partially coupled problems [33] or in other words, involves computation of the wavenumbers associated with the axial-bending (method reported in Ref. [3]), axial-torsion and torsion-bending cases separately. Characteristic systems arising from these partially coupled problems are essentially the submatrices of $\mathbf{F}(k)$. We compute the trial roots of Eq. (30) by averaging the wavenumbers obtained from the k subspaces explained above. Note that the operation is performed for each FFT sampling frequency ω_n (typically at 512 to 32 768 points depending on the resolution of the load history). Starting with trial roots to solve Eq. (30) reduces the number of iterations significantly. For refinement of the roots, IMSL© routine [37] based on Muller's method is called in the general purpose spectral FE code, followed by reordering of the wavenumbers to track individual propagating and evanescent wave modes over a broad frequency band. In cases where exact solution to the wavenumbers k_j^* are known, an approximation error in vibration modes can be obtained as

$$\delta = |1 - \mathrm{e}^{\mathrm{i}(k_j^* - k_j)h}|. \tag{31}$$

In short-wave regime (wavelength $\lambda_j = 2\pi/k_j$ small), where wave amplitudes are in the order of h, error estimate in dynamics of thin-walled bodies by perturbation of symmetric and antisymmetric thickness shear modes has been developed by Kaplunov et al. [25]. However, similar numerical error estimation in the present framework of spectral element development is beyond the scope of this paper and can be discussed elsewhere.

Wavenumber dispersion curves are now plotted in Fig. 2 for a AS/3501-6 graphite–epoxy composite tubular cross-section with fiber angle $\theta = 0^\circ$, $h = 0.002$ m, $\eta = h/R = 0.1$. The following material properties are used: elastic moduli: $E_{11} = 144.48$ GPa, $E_{22} = 9.632$ GPa, $E_{33} = 9.412$ GPa, $G_{23} = 6.516$ GPa, $G_{13} = 7.457$ GPa, $G_{12} = 4.128$ GPa; the Poissons ratio: $\nu_{23} = 0.49$, $\nu_{13} = 0.3$, $\nu_{12} = 0.3$ and density: $\rho = 1389.2$ kg/m^3. In Fig. 2, only the positive wavenumbers (forward propagating and evanescent modes) are plotted. Whereas, the negative wavenumbers with same amplitudes also exist and they represent backward propagating or evanescent modes. One order-of-scale difference between the wavenumbers associated with propagating axial, shear and propagating flexural, torsional modes can be seen. The plot also shows that at any material point, there will be additional propagating shear wave modes due to shear deformations γ_{xz} and γ_{xy} above the respective cut-off frequencies. The cut-off frequencies satisfy $\mathrm{Det}\,\mathbf{F}(0) = 0$. Below these cut-off frequencies, the shear waves are evanescent in nature.

3. Spectral finite element model

To represent all the wave coefficients in terms of only 12 primary unknown coefficients associated with three translational and three rotational motions, an amplitude ratio matrix $\mathbf{R}_{(6\times12)}$ is introduced in Eq. (28). Here, $R_{mj}\tilde{u}_j$ represents the entries in actual wave coefficient vector

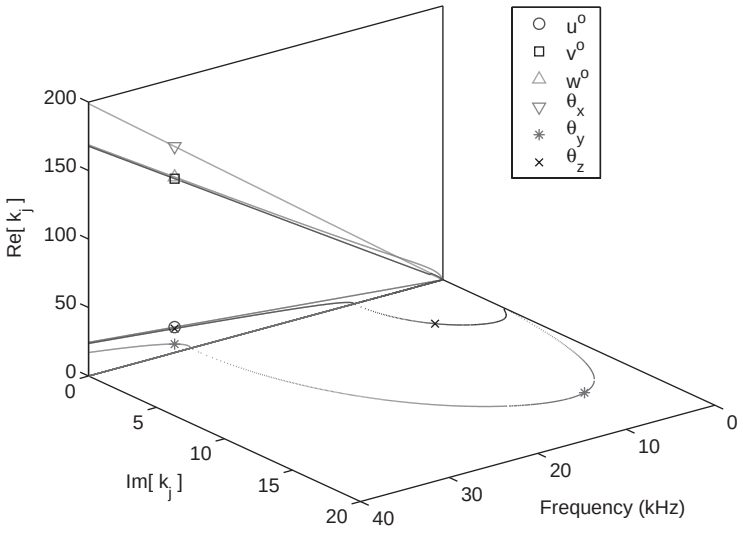

Fig. 2. Plot of wavenumbers k_j for a AS/3501-6 graphite–epoxy composite tubular cross-section with fiber angle $\theta = 0^\circ$, $h = 0.002$ m, $\eta = h/R = 0.1$.

associated with jth mode of propagation ($j = 1, \ldots, 12$) contributing in mth displacement component ($m = 1, \ldots, 6$). The vector $\mathbf{R}_j$, which forms the jth column of $\mathbf{R}$ is obtained by satisfying the equations

$$\mathbf{F}(k_j)\mathbf{R}_j = 0, \tag{32}$$

$$R_{mj} = 1 \quad \forall\{2(m-1)+1 = j \text{ or } 2(m-1)+2 = j\}. \tag{33}$$

After some algebraic manipulations, the above two equations yield the following system of linear equations to be solved at each ω_n:

$$\begin{bmatrix} F^j_{11} & \cdots & F^j_{1(m-1)} & F^j_{1(m+1)} & \cdots & F^j_{16} \\ \vdots & \ddots & \vdots & \vdots & \ddots & \vdots \\ F^j_{(m-1)1} & \cdots & F^j_{(m-1)(m-1)} & F^j_{(m-1)(m+1)} & \cdots & F^j_{(m-1)6} \\ F^j_{(m+1)1} & \cdots & F^j_{(m+1)(m-1)} & F^j_{(m+1)(m+1)} & \cdots & F^j_{(m+1)6} \\ \vdots & \ddots & \vdots & \vdots & \ddots & \vdots \\ F^j_{61} & \cdots & F^j_{6(m-1)} & F^j_{6(m+1)} & \cdots & F^j_{66} \end{bmatrix} \begin{Bmatrix} R_{1j} \\ \vdots \\ R_{(m-1)j} \\ R_{(m+1)j} \\ \vdots \\ R_{6j} \end{Bmatrix} = -\begin{Bmatrix} F^j_{1m} & \cdots & F^j_{(m-1)m} & F^j_{(m+1)m} & \cdots & F^j_{6m} \end{Bmatrix}^{\mathrm{T}}, \tag{34}$$

where $\mathbf{F}^j = \mathbf{F}(k_j)$. Relative magnitude of different amplitude ratios R_{mj} ($\leqslant 1$) represents whether a particular wave mode is strong or weak with respect to jth mode. Also, they capture the coupling among longitudinal, flexural and torsional motions.

We eliminate the 12 unknown wave coefficients in $\{\tilde{u}\}$ using six displacement boundary and six force boundary equations. Two nodes, each placed at the center of the tube end cross-sections

appear sufficient. Therefore, by evaluating Eq. (28) at the element nodes at $(0,0,0)$ and $(L,0,0)$, the element nodal displacement vector can be obtained as

$$\hat{\mathbf{u}}^e = \begin{bmatrix} \mathbf{T}_1(0,\omega_n) \\ \mathbf{T}_1(L,\omega_n) \end{bmatrix} \tilde{\mathbf{u}} = \mathbf{T}_2 \tilde{\mathbf{u}}, \tag{35}$$

where the non-singular (12×12) complex matrix $\mathbf{T}_2$ represents the local wave characteristics of displacement field. Combining Eqs. (28) and (35), shape function matrix $\aleph^e$, which is common in standard FE is obtained as

$$\hat{\mathbf{u}}(x,\omega_n) = \mathbf{T}_1(x,\omega_n)\mathbf{T}_2^{-1}\hat{\mathbf{u}}^e = \aleph(x,\omega_n)^e \hat{\mathbf{u}}^e. \tag{36}$$

The above equation can be used to obtain a strain–displacement matrix $\mathbf{B}^e$, which is a standard terminology in displacement-based FE approach, and can be derived here as

$$\begin{Bmatrix} \hat{\varepsilon}_{xx} \\ \hat{\gamma}_{xz} \\ \hat{\gamma}_{xy} \end{Bmatrix} = \begin{bmatrix} \dfrac{\partial}{\partial x} & 0 & 0 & 0 & \bar{z}\dfrac{\partial}{\partial x} & \bar{y}\dfrac{\partial}{\partial x} \\ 0 & 0 & \dfrac{\partial}{\partial x} & y\dfrac{\partial}{\partial x} & \dfrac{\partial \bar{z}}{\partial z} & \dfrac{\partial \bar{y}}{\partial z} \\ 0 & \dfrac{\partial}{\partial x} & 0 & z\dfrac{\partial}{\partial x} & \dfrac{\partial \bar{z}}{\partial y} & \dfrac{\partial \bar{y}}{\partial y} \end{bmatrix} \aleph(x,\omega_n)^e \hat{\mathbf{u}}^e = \mathbf{B}^e \hat{\mathbf{u}}^e. \tag{37}$$

Note that the exact strain field and stress field can be post-processed efficiently in closed form with the help of Eq. (37). Next, the relationship between generic displacement vector $\hat{\mathbf{u}}(x,\omega_n)$ and wave coefficient vector $\tilde{\mathbf{u}}$ in Eq. (28) is used to derive the generic force vector $\hat{\mathbf{f}}(x,\omega_n)$ from the force boundary conditions (Eqs. (21)–(26)) and is given by

$$\hat{\mathbf{f}}(x,\omega_n) = \mathbf{Q}_0 \mathbf{R} \Lambda_0 \tilde{\mathbf{u}} + \mathbf{Q}_1 \mathbf{R} \Lambda_1 \tilde{\mathbf{u}}, \tag{38}$$

where

$$\mathbf{Q}_0 = \begin{bmatrix} 0 & 0 & 0 & 0 & (A_{1519} + A_{1618}) & (A_{1517} + A_{1616}) \\ 0 & 0 & 0 & 0 & (A_{5619} + A_{6618}) & (A_{5617} + A_{6616}) \\ 0 & 0 & 0 & 0 & (A_{5519} + A_{5618}) & (A_{5517} + A_{5616}) \\ 0 & 0 & 0 & 0 & \begin{pmatrix} A_{5529} + A_{5628} \\ -A_{5639} - A_{6638} \end{pmatrix} & \begin{pmatrix} A_{5527} + A_{5626} \\ -A_{5637} - A_{6636} \end{pmatrix} \\ 0 & 0 & 0 & 0 & (A_{1559} + A_{1658}) & (A_{1557} + A_{1656}) \\ 0 & 0 & 0 & 0 & (A_{1549} + A_{1648}) & (A_{1547} + A_{1646}) \end{bmatrix}, \tag{39}$$

$$\mathbf{Q}_1 = \begin{bmatrix} A_{1111} & A_{1611} & A_{1511} & (A_{1512} - A_{1613}) & A_{1115} & A_{1114} \\ & A_{6611} & A_{5611} & (A_{5612} - A_{6613}) & A_{1615} & A_{1614} \\ & & A_{5511} & (A_{5512} - A_{5613}) & A_{1515} & A_{1514} \\ & \textit{Sym.} & & \begin{pmatrix} A_{5522} - 2A_{5623} \\ +A_{6633} \end{pmatrix} & \begin{pmatrix} A_{1525} \\ -A_{1635} \end{pmatrix} & \begin{pmatrix} A_{1524} \\ -A_{1634} \end{pmatrix} \\ & & & & A_{1155} & A_{1145} \\ & & & & & A_{1144} \end{bmatrix}. \tag{40}$$

Λ_1 is a (12×12) diagonal matrix obtained as

$$\Lambda_{1jj} = \frac{\partial}{\partial x}\Lambda_{0jj}, \quad i = 1, \ldots, 12. \tag{41}$$

By evaluating Eq. (41) at the element nodes placed at $(0,0,0)$ and $(L,0,0)$ and by substituting $\tilde{\mathbf{u}}$ using Eq. (35), the element nodal force vector $\hat{\mathbf{f}}^e$ is related to the element nodal displacement vector $\hat{\mathbf{u}}^e$ as

$$\hat{\mathbf{f}}^e = \begin{bmatrix} -(\mathbf{Q}_0\mathbf{R}\Lambda_0 + \mathbf{Q}_1\mathbf{R}\Lambda_1)_{x=0} \\ \\ (\mathbf{Q}_0\mathbf{R}\Lambda_0 + \mathbf{Q}_1\mathbf{R}\Lambda_1)_{x=L} \end{bmatrix} \mathbf{T}_2^{-1}\hat{\mathbf{u}}^e = \hat{\mathbf{K}}^e\hat{\mathbf{u}}^e. \tag{42}$$

Here, $\hat{\mathbf{K}}^e$ is a (12×12) complex dynamic stiffness matrix for the spectral FE.

3.1. Elements with absorbing boundary: throw-off spectral element

Since the element nodal vectors are obtained explicitly in a systematic manner (Eq. (29)), it becomes possible to identify the boundary reflection terms in the displacement, strain, stress, etc. This particular aspect is helpful when one needs to exclude the effect of wave scattering at structural boundaries or to filter out any noise from nearfield response. In the proposed SFEM, such an analytical feature of a single-node semi-infinite throw-off spectral element is implemented by assigning $L = \infty$ in Eq. (35) and by modifying the amplitude ratio matrix as

$$\mathbf{R} = \begin{bmatrix} R_{11} & 0 & R_{13} & 0 & R_{15} & 0 & R_{17} & 0 & R_{19} & 0 & R_{1\,11} & 0 \\ \vdots & 0 & \vdots & 0 & \vdots & 0 & \vdots & 0 & \vdots & 0 & \vdots & 0 \\ R_{61} & 0 & R_{63} & 0 & R_{65} & 0 & R_{67} & 0 & R_{69} & 0 & R_{6\,11} & 0 \end{bmatrix}. \tag{43}$$

Use of this throw-off element at the structural boundary amounts to absorption of all the energy from the structure and hence maximum damping artificially introduced to the response.

3.2. Computational issues

After transforming the element local system (Eq. (42)) into the global structural system and assembling in the global dynamic stiffness matrix, we need to solve it at each FFT sampling frequency ω_n. Apart from this major difference compared to time stepping or computation-intensive modal analysis in standard FE solutions, the proposed SFEM becomes very efficient in

terms of system size. This is evident from the above derivations that the exact solution to the wave equation inherited in Eq. (42) allows one to consider a single element over uniform spatial domain. Hence, broadband wave propagation analysis to obtain frequency responses as well as time responses in a large structures made of several of similar composite elements becomes highly automated and computationally much cheaper. However, additional complexities in wavenumber computation and inversion of $\mathbf{T}_2$ using matrix domain decomposition techniques to speed up computation need further optimization.

Once the global dynamic system is formed with the help of Eq. (42), frequency response function (FRF) can be computed by inverting the dynamic stiffness matrix directly due to its small size. We solve the system for unit spectral amplitudes of the load histories

$$\mathbf{f}(x,t) = \sum_{n=1}^{N} \hat{\mathbf{f}}(x,\omega_n)\, \mathrm{e}^{\mathrm{i}\omega_n t} \tag{44}$$

at the spectral element nodes. Actual response is computed and post-processed by convolving the spectral amplitude of the load. Only the dynamic stiffness matrix at each frequency needs to be stored if repeated analysis is required for various non-stationary load histories. In most general cases while analyzing a composite network or skeletal structure where the element material property sets are more than one, wavenumbers can be stored for each material property set and nodal displacement (as few as the number of global interconnections or structural joints) need to be stored for any post-processing and other complicated analysis.

3.3. Short- and long-wavelength limits for thin shell and limitations of the proposed model

From the kinematic assumptions (Eqs. (1)–(3)) in the proposed higher order cylindrical bending model, it is clear that there are restrictions for using this model for wave propagation in very thin as well as very thick shell. Typically, for thin shell, one would expect the shell transverse motion as predominant one compared to that due to bending rotation of the shell cross-section. In thin cylindrical shell, therefore, the axisymmetric radial motion becomes important. On the other hand, in thick cylindrical shell, one would expect the propagation of higher order Lamb wave modes (first and higher symmetric stretching modes, and third and higher antisymmetric modes) apart from propagating longitudinal, flexural and shear wave modes. For thick cylindrical shell, therefore, the spectral band should be limited below the cut-off frequencies of the higher order Lamb wave modes that are not included in the kinematics of the present model. The short- and long-wavelength limits for thin shell (based on Love's thin-shell theory), beyond which, significant deviation of the proposed model from the actual behavior may occur, are discussed below.

Let us consider a cylindrical thin shell segment as shown in Fig. 3, where u, v and w are the longitudinal, tangential and radial displacements, respectively. By neglecting the effect of bending moment, transverse shear deformation and rotation of the shell normal, the thin-shell kinematics [38] can be written as

$$\varepsilon_{xx} = u_{,x}\,, \quad \varepsilon_{\phi\phi} = \frac{1}{R}(w + v_{,\phi}), \quad \gamma_{x\phi} = v_{,x} + \frac{1}{R}u_{,\phi}\,. \tag{45}$$

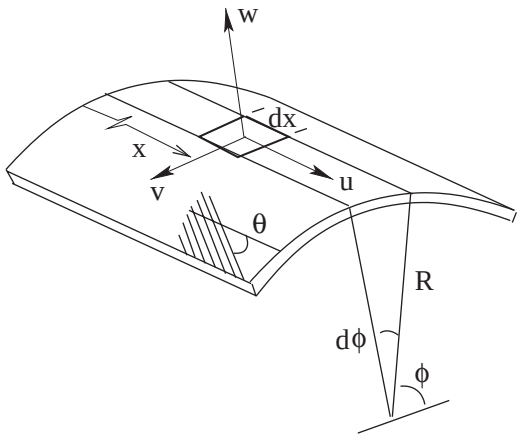

Fig. 3. Co-ordinate system and d.o.f.'s for laminated composite thin shell ($h \ll R$).

The orthotropic constitutive model in ply-local co-ordinate system can be expressed as

$$\begin{Bmatrix} \sigma_{xx} \\ \sigma_{\phi\phi} \\ \tau_{x\phi} \end{Bmatrix} = \begin{bmatrix} \bar{Q}_{11} & \bar{Q}_{12} & \bar{Q}_{16} \\ \bar{Q}_{12} & \bar{Q}_{22} & \bar{Q}_{26} \\ \bar{Q}_{16} & \bar{Q}_{26} & \bar{Q}_{66} \end{bmatrix} \begin{Bmatrix} \varepsilon_{xx} \\ \varepsilon_{\phi\phi} \\ \gamma_{x\phi} \end{Bmatrix}. \tag{46}$$

Substituting Eqs. (45) and (46) in the energy components and applying Hamilton's principle, the coupled wave equations for the composite thin shell can be expressed as

$$-I_0\ddot{u} + \bar{A}_{11}u_{,xx} + \bar{A}_{12}\frac{1}{R}(w_{,x} + v_{,x\phi}) + \bar{A}_{26}\frac{1}{R^2}(w_{,\phi} + v_{,\phi\phi}) + \bar{A}_{16}\left(\frac{2}{R}u_{,x\phi} + v_{,xx}\right) + \bar{A}_{66}\frac{1}{R}\left(v_{,x\phi} + \frac{1}{R}u_{,\phi\phi}\right) = 0, \tag{47}$$

$$-I_0\ddot{v} + \bar{A}_{12}\frac{1}{R}u_{,x\phi} + \bar{A}_{22}\frac{1}{R^2}(w_{,\phi} + v_{,\phi\phi}) + \bar{A}_{16}u_{,xx} + \bar{A}_{26}\frac{1}{R}(w_{,x} + 2v_{,x\phi} + u_{,\phi\phi}) + \bar{A}_{66}\left(v_{,xx} + \frac{1}{R}u_{,x\phi}\right) = 0, \tag{48}$$

$$I_0\ddot{w} + \bar{A}_{12}\frac{1}{R}u_{,x} + \bar{A}_{22}\frac{1}{R^2}(w + v_{,\phi}) + \bar{A}_{26}\frac{1}{R}v_{,x} = 0, \tag{49}$$

where

$$(\bar{A}_{jl}, I_0) = \int_{-h}^{+h} (\bar{Q}_{jl}, \rho)\,\mathrm{d}z. \tag{50}$$

To obtain the characteristic equation, the spectral form of the displacement variables $\mathbf{u} = \{u,\ v,\ w\}^{\mathrm{T}}$ in k-space can be assumed, which is

$$\mathbf{u} = \sum \hat{\mathbf{u}}(\phi)\mathrm{e}^{-\mathrm{i}(kx-\omega_n t)}, \tag{51}$$

where k is the wavenumber in the longitudinal direction. For displacement continuity of the circumferential motion, $\hat{\mathbf{u}}(\phi) = \hat{\mathbf{u}}(2\pi + \phi)$. Therefore, for circumferential wave propagation, we can write

$$\mathbf{u} = \sum \tilde{\mathbf{u}}(\phi) e^{-i(kx+\gamma\phi-\omega_n t)}, \tag{52}$$

where γ is the integer wavenumber in tangential direction. The coupling between the longitudinal and tangential modes for different fiber angles θ (Fig. 3) is preserved through the wave coefficient vector $\tilde{\mathbf{u}}$. Substituting Eq. (52) in the thin-shell wave Eqs. (47)–(49), the characteristic equation becomes

$$\text{Det } \mathbf{G}(k, \gamma) = 0. \tag{53}$$

Since our objective here is to draw the restriction of the proposed model as the shell becomes very thin, $h \ll R$, the fundamental axisymmetric modes and pure tangential modes need to be studied in the limits of short and long wavelengths.

The fundamental axisymmetric modes (longitudinal and radial) and vanishing tangential mode are recovered from Eq. (53) by substituting $\eta = 0$ and solving for k. In this case, we get a fourth order characteristic equation in k given by

$$ak^4 + bk^2 + c = 0, \tag{54}$$

where

$$a = \omega_n^2 I_0(-\bar{A}_{11}\bar{A}_{66} + \bar{A}_{16}^2) + \frac{1}{R^2}(\bar{A}_{11}\bar{A}_{22}\bar{A}_{66} - \bar{A}_{11}\bar{A}_{26}^2 - \bar{A}_{16}^2\bar{A}_{22} + 2\bar{A}_{12}\bar{A}_{16}\bar{A}_{26} - \bar{A}_{12}^2\bar{A}_{66}), \tag{55}$$

$$b = \omega_n^4 I_0^2(A_{66} + A_{66}) - \omega_n^2 I_0 \frac{1}{R^2}(A_{11}A_{22} + A_{22}A_{66} - A_{12}^2 - A_{26}^2), \tag{56}$$

$$c = -\omega_n^6 I_0^3 + \omega_n^2 I_0 \frac{1}{R^2} A_{22}. \tag{57}$$

In the short-wavelength limit, $k \to \infty \Rightarrow a = 0$,

$$\Rightarrow \omega_s = \omega_n = \left[\frac{(A_{11}A_{22} - A_{12}^2)A_{66} + 2A_{12}A_{16}A_{26} - A_{11}A_{26}^2 - A_{22}A_{16}^2}{R^2 I_0(A_{11}A_{66} - A_{16}^2)}\right]^{1/2} \tag{58}$$

is the frequency at which the wave dispersion has singularity. That is the cylinder experiences resonance at ω_s in the axisymmetric radial mode. In the long-wavelength limit, $k \to 0 \Rightarrow c = 0$

$$\Rightarrow \omega_l = \omega_n = 0, \quad \frac{1}{R}\sqrt{\frac{A_{22}}{I_0}} \tag{59}$$

is the frequency after which the axisymmetric radial mode again starts propagating and is also the cut-off frequency for axisymmetric wave propagating in thin shell. For isotropic case, this becomes $(1/R)\sqrt{E/\rho(1-\nu^2)}$ and is called the ring frequency, which has been discussed in the introductory discussion. Also, for isotropic case, ω_s becomes simply $(1/R)\sqrt{E/\rho}$ and smaller than the ring frequency. Hence, for isotropic as well as orthotropic materials, it can be said that, the axisymmetric radial mode first becomes resonant at ω_s and cease to propagate and then again

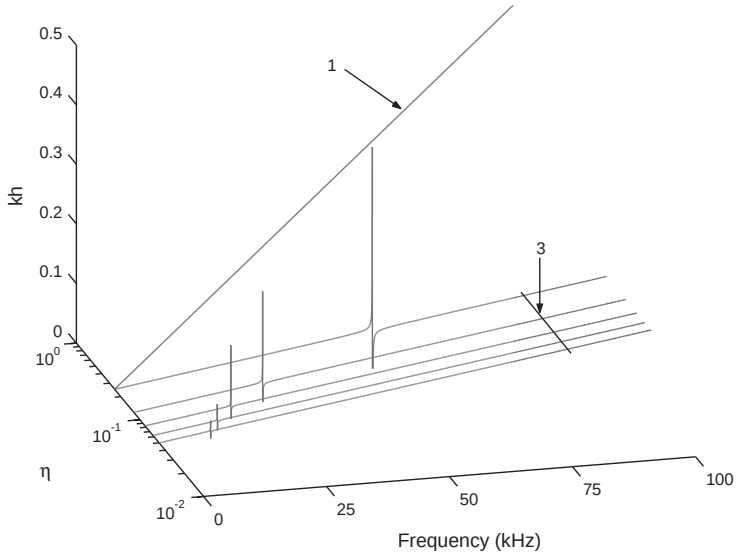

Fig. 4. Plot of wavenumbers in axisymmetric modes (1—longitudinal, 3—radial) for different $\eta(=h/R)$ (0.05–0.25) for $\theta = 0^\circ$ AS/3501-6 graphite–epoxy composite shell.

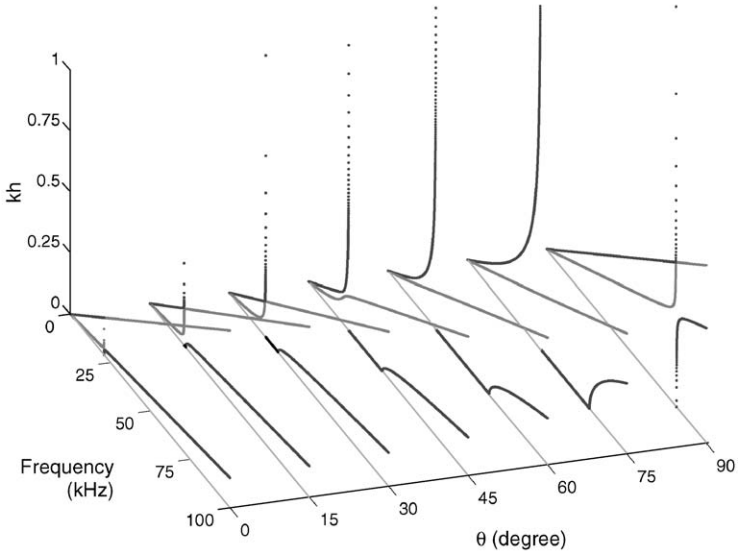

Fig. 5. Plot of wavenumbers in axisymmetric modes (1—longitudinal, 3—radial) for different fiber angles θ for $\eta = 0.1$ $h = 2$ mm AS/3501-6 graphite–epoxy composite shell.

starts propagating at little higher frequency, that is at ω_l. For $h = 2$ mm, $\eta = 0.1$ as considered in Fig. 2, these limiting frequencies are $\omega_s = 20.954$ kHz and $\omega_l = 21.017$ kHz. Fig. 4 shows the location of the singularity and cut-off in the axisymmetric radial mode (marked 3) in a graphite–epoxy composite shell with different $\eta(=h/R)$ and $\theta = 0$. The non-dispersive longitudinal modes (marked 1) remain unchanged for all values of η. Fig. 5 shows the separation between the

singularity (ω_s on the lower side along the frequency axis) and the cut-off following new propagation of the axisymmetric radial mode (ω_l on the higher side along the frequency axis). Therefore, to exclude the effect of unaccounted radial mode (as in case of the proposed new tubular element), the best comparable behavior of cylindrical tube (when modelled as beam) can be obtained for certain range of η, such that the applied forcing frequency band falls below $\omega_s < \omega_l$. And, as a special case for certain orientation of the fibers, a second frequency band between ω_s and ω_l (Fig. 5) can be obtained, within which the axisymmetric radial mode vanishes. This can be clearly seen from Fig. 6, which shows that almost 35 kHz bandwidth is available with vanishing axisymmetric radial mode for a tube cross-section having $\eta = 0.1$ and fiber angle $\theta = 60^\circ$. This is the so called stop band for radial mode, which is an important design parameter for composite shells for controlling vibration and buckling. However, it should be noted that for the composite tube when designed to behave mainly as a thin-walled beam structure, the beam motion is less likely to be affected by the radial mode (as the motion of the beam axis remains unaltered), unless a circumferential normal pressure type loading is applied.

The fundamental cross-sectional warping mode consisting of coupled torsional–radial motion is recovered by substituting $k = 0$ in Eq. (53) and solving the fourth order polynomial in γ given by

$$a'\gamma^4 + b'\gamma^2 + c' = 0, \tag{60}$$

where

$$a' = -\omega_n^2 I_0 \frac{1}{R^4} A_{22} A_{66} + \omega_n^2 I_0 \frac{1}{R^3} A_{26}^2, \tag{61}$$

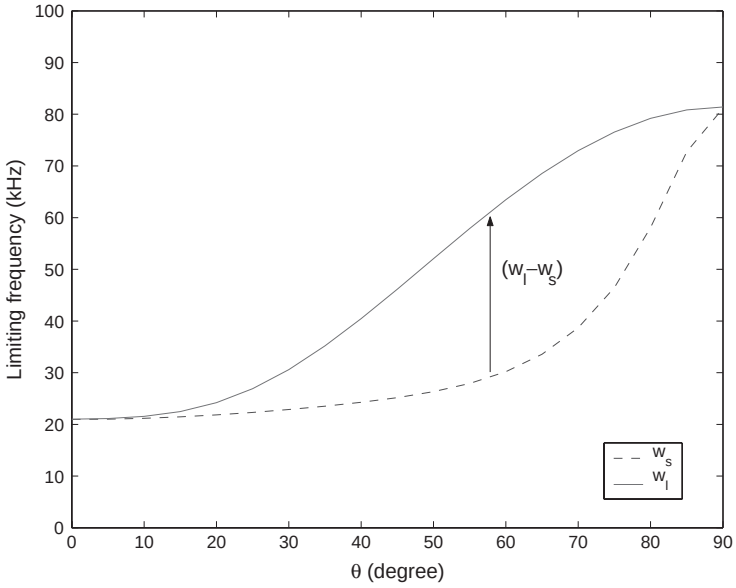

Fig. 6. Separation between the short- and long-wave limiting frequencies ($\omega_l - \omega_s$) for different fiber angles θ for $\eta = 0.1$, $h = 2$ mm AS/3501-6 graphite–epoxy composite shell.

$$b' = \omega_n^4 I_0^2 \frac{1}{R^2}(A_{22} + A_{66}) - \omega_n^2 I_0 \frac{1}{R^4} A_{22}A_{66}, \tag{62}$$

$$c' = -\omega_n^6 I_0^3 + \omega_n^4 I_0^2 \frac{1}{R^2} A_{22}. \tag{63}$$

In the short-wavelength limit, $\gamma \to \infty \Rightarrow a' = 0$

$$\Rightarrow \omega_s = \omega_n = 0 \quad \text{or} \quad R = \frac{A_{22}A_{66}}{A_{66}^2} \to \infty, \tag{64}$$

which shows that for smaller radius of the cylindrical tube, the wavelength of radial mode becomes longer and vanishes below the long-wavelength limit ω_l, which is also the cut-off frequency for such propagation. This long-wavelength limit is obtained for $\gamma \to 0 \Rightarrow c' \to 0$

$$\Rightarrow \omega_l = \omega_n = 0, \quad \frac{1}{R}\sqrt{\frac{A_{22}}{I_0}}, \tag{65}$$

which is same as the cut-off frequency of the radial mode in axisymmetric case (Eq. (59)). Fig. 7 shows the decreasing nature of γ (hence increasing wavelengths) for the tangential and radial modes for increasing η. Also, the cut-off frequency of the radial modes shift towards higher frequency range for increasing η (smaller radius for a given shell thickness). Fig. 8 shows similar shift in the cut-off frequency of radial mode (as in the above case) for increasing fiber angles θ for $\eta = 0.1$. However, the tangential or torsional mode has a symmetry about $\theta = 45^\circ$ and is non-dispersive. Such cross-sectional warping is already present in the proposed model (see the kinematics), where propagation of the radial mode induced by torsional load is not restricted due to any additional kinematical assumptions.

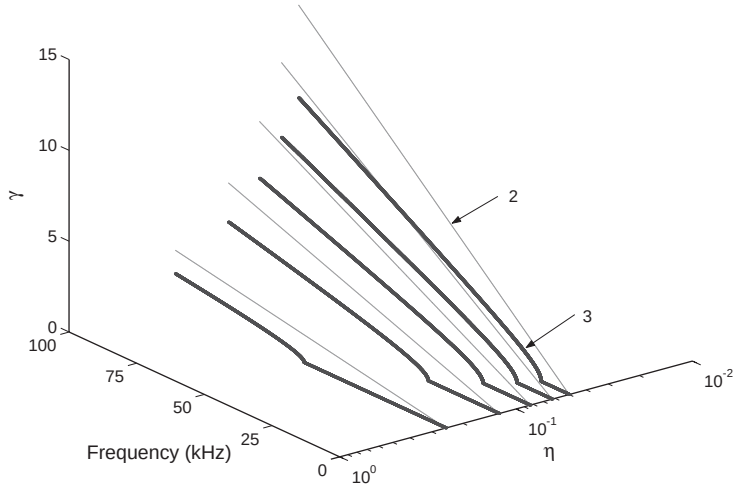

Fig. 7. Plot of wavenumbers in tangential–radial modes (2—tangential, 3—radial) for different $\eta(= h/R)$ (0.05–0.25) for $\theta = 0^\circ$ AS/3501-6 graphite–epoxy composite shell. Only integer values of the wavenumbers γ are admissible.

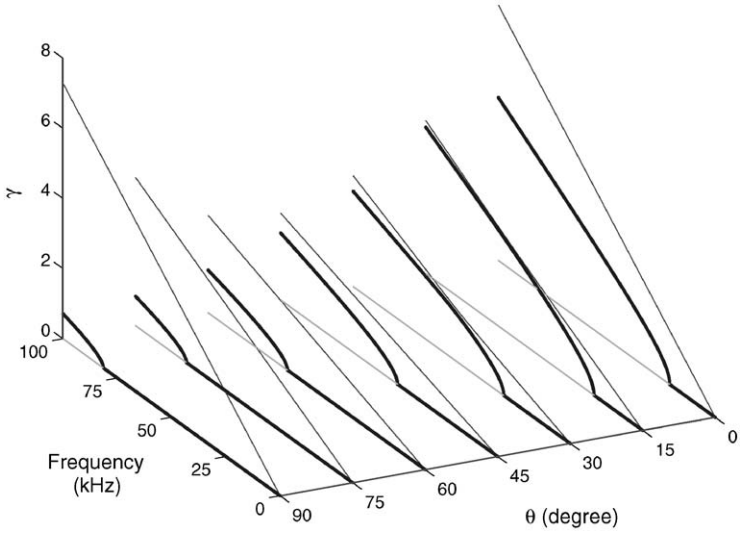

Fig. 8. Plot of wavenumbers in tangential–radial modes (2—tangential, 3—radial) for different fiber angles θ for $\eta = 0.1$, $h = 2$ mm AS/3501-6 graphite–epoxy composite shell. Only integer values of the wavenumbers γ are admissible.

The above analysis shows that the main limitation of the proposed tubular element while capturing the behavior of composite thin cylindrical shell is that the axisymmetric radial mode induced by longitudinal load is absent in the element. Also, the circumferential normal pressure load on the cylindrical cross-section cannot be modelled. The best comparable thin-shell behavior can be captured over frequency band below the limiting frequency of short wavelength ω_s and over the stop bands $(\omega_l - \omega_s)$ for specified values of $\eta(= h/R)$ and fiber angle θ for axisymmetric modes. On the higher side of η and smaller L/R, one needs to consider the effect of parabolic transverse shear stress variation across the shell thickness and vanishing normal stress at the shell surfaces in the kinematics, which are not included in the present model. Therefore, for accurate results, application of the present tubular element needs to be restricted for forcing frequency bandwidth below the lowest of the new cut-off frequencies of any of these un-accounted modes (i.e., higher order antisymmetric Lamb wave mode due to parabolic transverse shear and symmetric Lamb wave mode due to vanishing normal stress at the shell surfaces). However, it can be seen that for both the axisymmetric as well as torsional excitations in very thick cylindrical shell and rod [10], the lowest longitudinal and torsional modes remain non-dispersive and they are preserved in the present model. The studies on characteristic wave behavior reported in Ref. [11] for higher thickness and anisotropy can be adopted to draw the thickness limit for particular application while using the present SFEM.

3.4. Comparison with analytical solution

Although many theories based on potential functions as well as first order and higher order shear deformable shell kinematics have been reported in literature as discussed earlier, most of the wave propagation studies are focused on the analysis of the frequency spectrum and harmonic analysis in modal space and are difficult to apply for transient dynamic analysis. For validation of

the results from the present SFEM, which is mainly suited for broadband and impact-type loading on composite tubes, we consider the analytical solution for impact-induced response of a semi-infinite membrane shell [38] for unidirectional ($\theta = 0^\circ$) composite. The kinematics is given in Eq. (45). Additional approximations that can be made under longitudinal impact is $\partial/\partial\phi(\,) = 0$ and $v \to 0$. Starting with shear deformable kinematics also, the same approximation remains valid (except near structural boundaries across the span) under longitudinal impact, and the wave equations take the form

$$-I_0\ddot{u} + A_{11}u_{,xx} + A_{12}\frac{1}{R}w_{,x} = 0, \tag{66}$$

$$I_0\ddot{w} + A_{12}\frac{1}{R}u_{,x} + A_{22}\frac{1}{R^2}w = 0, \tag{67}$$

subjected to initial condition $\dot{u}(x,0) = 0$ at $t = 0$, the boundary conditions $u = u(x,t)$ and $w = w(x,t)$ prescribed at a particular x or

$$-A_{11}u_{,x} - A_{12}\frac{1}{R}w = N_x, \tag{68}$$

where N_x is the applied longitudinal impact. Assuming the solution of the field variables $\mathbf{u}$ transformed into their time uncoupled Fourier coefficients (spectral amplitude) $\hat{\mathbf{u}}$ as done earlier, we can write

$$u = \sum_n \hat{u}e^{i\omega_n t}, \quad \hat{u} = \tilde{u}_1 e^{-i\bar{k}x} + \tilde{u}_2 e^{i\bar{k}x}, \tag{69}$$

$$w = \sum_n \hat{w}e^{i\omega_n t}, \quad \hat{w} = \tilde{w}_1 e^{-i\bar{k}x} + \tilde{w}_2 e^{i\bar{k}x}, \tag{70}$$

where the wavenumber

$$\bar{k} = \sqrt{\frac{\omega_n^2 I_0(1/R^2)A_{22} - \omega_n^4 I_0^2}{\omega_n^2 I_0 A_{11} - (A_{11}A_{22} - A_{12}^2)(1/R^2)}}, \tag{71}$$

is obtained by solving the characteristic equation derived from Eqs. (66) and (67). ω_n is the fine sampling frequency used for forward and inverse FFT and same as the sampling frequency of the impact loading spectrum $\hat{N}_x(\omega_n)$ (Eq. (44)) used to excite the structure. Considering the free-end of the semi-infinite complete cylindrical membrane shell under impact load is at $x = L$ and the other end is at $x = -\infty$, the displacement spectrum $\hat{u}$ finally becomes

$$\hat{u} = \tilde{u}_1 e^{-i\bar{k}x}, \quad \tilde{u}_1 = \frac{\hat{N}_x/(2\pi R)}{(-i\bar{k}A_{11} + A_{12}(1/R)R_{21})e^{-i\bar{k}L}}, \tag{72}$$

where

$$R_{21} = \frac{-iA_{12}(1/R)\bar{k}}{-\omega^2 I_0 + A_{22}(1/R^2)}. \tag{73}$$

The short-impulse-type loading used for longitudinal impact is shown in Fig. 9. The time duration is approximately 50 μs with peak amplitude of 100 N. The load spectrum is shown in the inset of Fig. 9. Fine discretization of the frequency spectrum with Nyquist point $N = 16\,384$ ($\Delta t = 1$ μs) is

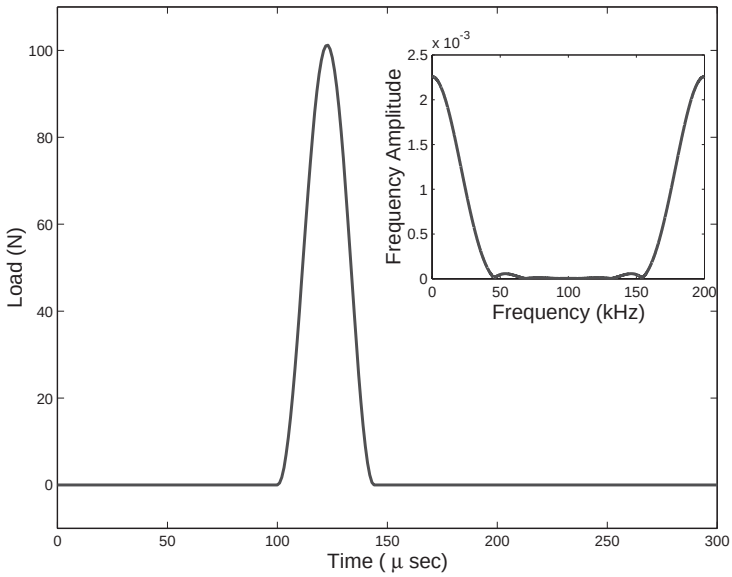

Fig. 9. A short-pulse load history used to excite the composite tubes. Frequency amplitudes at different frequencies are shown in the inset.

made while inverse FFT of analytically computed velocity spectrum $i\omega_n\hat{u}$ (Eq. (72)) to obtain the velocity history at $x = L$. Graphite–epoxy unidirectional composite ($\theta = 0^\circ$) with material properties as considered earlier is used here. The velocity history from analytical result is plotted in comparison with the velocity history from SFEM (using a single throw-off element as discussed in Section 3.1) in Fig. 10. It can be seen from the analytical result that the initial impact has produced non-dispersive longitudinal wave coupled with radial motion after the initial incidence. Although the tube is semi-infinite along x, the almost stationary axisymmetric radial motion has non-decaying effect, which has caused window distortion. This numerical problem inherent to the FFT is evident from the initial non-zero values in the analytical response before the initial incidence at around 100 μs (Fig. 9). The non-dispersive nature of the longitudinal velocity after incidence, which is due to coupling with radial motion, could not be captured by the SFEM as the degrees of freedom (d.o.f.'s) associated with axisymmetric radial motion is absent in the model. Also, the peak velocity estimate from SFEM is higher than that compared to the analytical result.

4. Numerical simulations

As discussed in the introductory discussion that many solution methods and fundamental studies have been reported in literature on wave propagation in cylindrical shells. Although few studies are on composite shells and thin-walled bodies, they are focused on the in-plane and flexural wave motions separately. However, due to wide tailorability of composite materials (ratios of elastic moduli in principal co-ordinates, the Poisson ratio, fiber orientations, inclusions, etc.), a single computational framework is necessary from engineering application point of view.

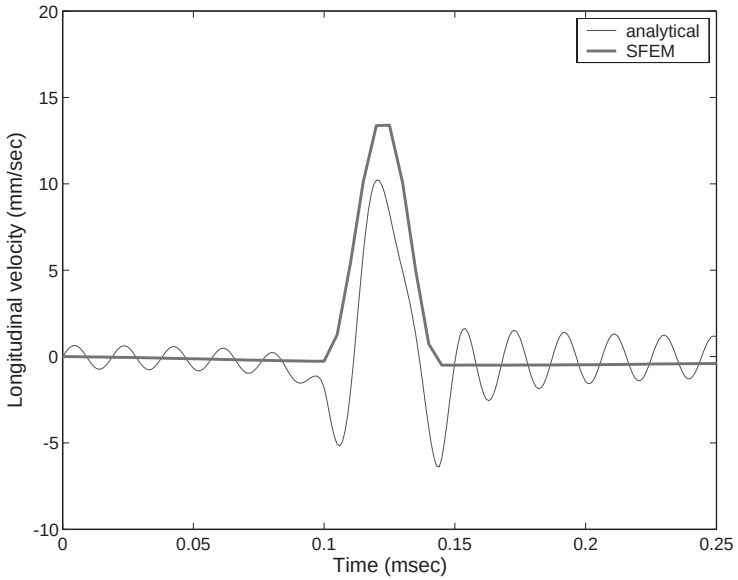

Fig. 10. Comparison of the mid-plane longitudinal velocity from SFEM and analytical result at the free end of a semi-infinite graphite–epoxy unidirectional ($\theta = 0^\circ$) composite membrane shell ($h = 0.002,\ h/R = 0.1$) under the short pulse (Fig. 9) applied in longitudinal direction.

The SFEM presented in the previous section is intended for such purpose. In this section, numerical simulations are carried out considering a single clamped–free graphite–epoxy tubular element. Before we analyze the nature of time response of such a structure under short-impulse load, it is worth looking at the resonant vibration modes among which the energy will be distributed.

4.1. Modal density distribution in wavelength and time scales

Since the dispersion relation for axial–flexural-torsion coupled wave propagation for the developed tubular element (uncoupled result is shown in Fig. 2) is not amenable in closed form, and are fairly complicated due to cut-off frequencies and cross-overs between each other, direct physical conclusions are difficult to draw. Instead, it appears useful to study the effect of wavelength and time scales on the dynamics. The importance of modal density distribution in k-space over the predictions of individual modes in broadband wave propagation problem has been discussed by Langley [17]. In the present context of coupled wave propagation, we take the notion of a variability index p and a dynamicity index q as proposed by Kaplunov et al. [25] to characterize the dynamics. These indices are defined as

$$\lambda_j/R = \eta^p, \quad \tau/(Rc_o^{-1}) = \eta^q, \tag{74}$$

where $\eta = h/R$ is a geometric parameter, $\lambda_j = 2\pi/k_j$ is the wavelength of the jth wave mode and $\tau = Rc_g^{-1}$ is the time scale as discussed in the introductory section. $c_o = \sqrt{A_{1111}/M_{11}}$ is the phase speed of primary axial wave in the tube as a thin-walled beam. If η is considered as a length scale

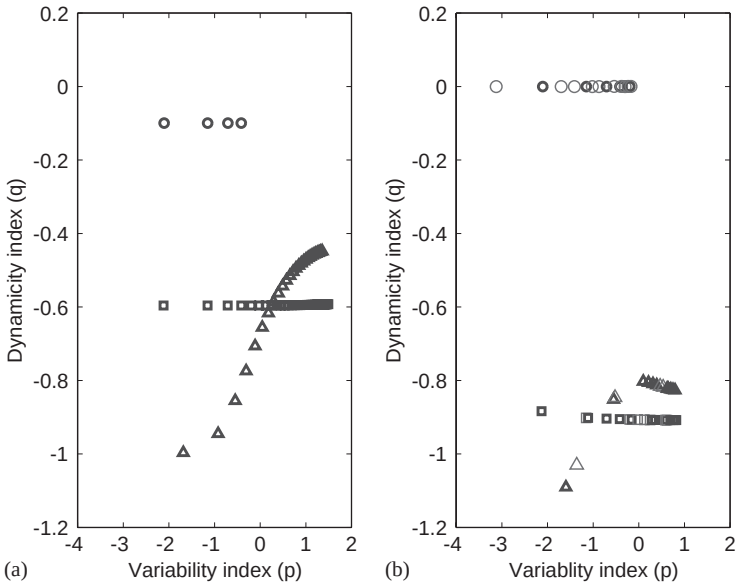

Fig. 11. Density distribution of vibrational modes in (p, q) co-ordinates (Eq. (74)) for a clamped–free graphite–epoxy composite tube with $h = 2$ mm, $\eta = 0.1$ and fiber angle (a) $\theta = 0^\circ$, (b) $\theta = 30^\circ$ over a frequency range of 20 kHz. ○, axial mode; △, transverse bending mode; □, torsional mode: The larger symbols in (b) represent coupled or secondary resonant modes.

to classify different types of wave, then $p \geqslant 1$ represents short-wave region, and subsequently, high-frequency dynamics can be experienced as q moves from $q < 1$ to $q = 1$.

To obtain the modal density distribution in (p, q) co-ordinate, first we identify the resonant frequencies from the location of the poles along frequency axis in the frequency response of displacements (axial, transverse and torsion) under unit impulse. For uncoupled motions ($\theta = 0^\circ$), all of these poles correspond to the natural frequency of the primary resonant vibrational modes in individual frequency response. For coupled motions ($\theta \neq 0^\circ$ in Fig. 1), the coupled or secondary resonant vibrational modes can be separated from the primary resonant vibrational modes due to their smaller spectral amplitudes $\hat{\mathbf{u}}$. Next, propagating wavelengths and group speeds corresponding to each of these resonant frequencies are computed to locate them in (p, q) co-ordinate using Eq. (74). Fig. 11(a) shows the modal density distribution of a clamped–free graphite–epoxy tube for $\theta = 0^\circ$, $\eta = 0.1$ and with same material properties as used earlier. It can be seen from the plot that the resonant axial and torsional vibration modes together represent always a low-frequency dynamics compared to the increasing nature of the high-frequency dynamics in resonant bending vibration modes. Higher modal densities of resonant bending and torsional vibration modes are visible in short-wave region. Fig. 11(b) shows the modal density distribution for $\theta = 30^\circ$. Here, it can be seen that the resonant bending and torsional vibration modes together represent a lower frequency dynamics compared to $\theta = 0^\circ$ case. On the other hand, the resonant axial modes moves towards higher frequency dynamics. Interaction in wavelength scale does not change much. However, the density of primary resonant vibration modes decreases and a number of secondary modes appear.

4.2. Time response under short-impulse load and the effect of fiber orientations

The short-impulse load history used to excite the clamped–free graphite–epoxy composite tube at its free end is shown in Fig. 9. The time duration is approximately 50 μs with peak amplitude of 100 N. The load spectrum has dominant frequency components up to 40 kHz. Such broadband also encompasses the propagating shear wave modes (see Fig. 2). We formulated the spectral element considering undamped system. However, in composite structures, damping is a common phenomena. Different approaches to include the effect of proportional and non-proportional damping in SFEM have been proposed in Ref. [34]. In the following simulations, we assume small amount of damping in the form $k_j \leftarrow k_j(1 - i\eta_d)$, where the damping coefficient (also called loss factor) $\eta_d = 0.001$. Also, improved numerical stability and reduced effect of frequency window distortion can be achieved by using such artificial damping in an undamped model when accurate time responses need to be post-processed.

First, we simulate the dynamic response of a clamped–free tube ($L = 1$ m, $L/R = 50$, $\eta = 0.1$, $\theta = 0^\circ$) by applying the above short pulse at the free end separately in global X and Z directions and similar moment of 100 N m about X-axis.

For load applied in X-direction, the deformed outer surface ($\xi = h$) geometry is snapped at $t = 0.5$ ms in Fig. 12. One limitation of the model is clearly visible from this simulation, that is the absence of any axisymmetric surface undulations on the axially compressed rings. Such small-scale effect can be obtained through general shell kinematics as discussed in Section 3.3. For three different sets of fiber angle, axial displacement and axial velocity histories at the point $(1, 0, R + h)$ on the free end are shown, respectively, in Figs. 13 and 14. After the initial incidence of the impact, repeated reflections from the clamped end of the tube can be seen in both the responses. It is interesting to note that the $\theta = [0^\circ]_{10}/[90^\circ]_{10}$ configuration, which generates maximum thickness asymmetry along local ξ direction, is less responsive compared to $\theta = [+45^\circ]_{10}/[-45^\circ]_{10}$ configuration.

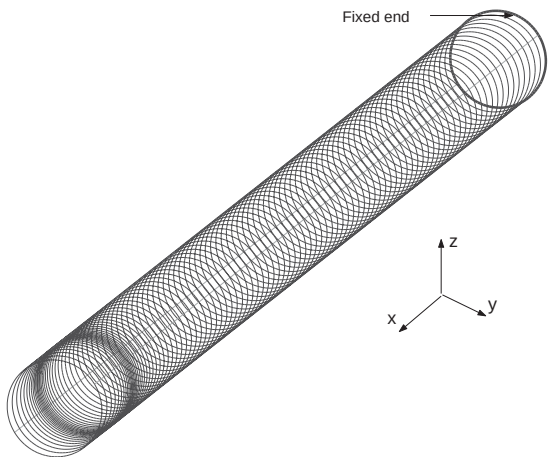

Fig. 12. Snap of the outer surface geometry at $t = 0.5$ ms for the graphite–epoxy composite clamped–free tube (L = 1 m, $L/R = 50$, $\eta = 0.1$ with $\theta = 0^\circ$ lay-up). A short-pulse load (Fig. 9) is applied uniformly at the free end along X-direction. Scale-factor for displacement amplification is 1×10^8.

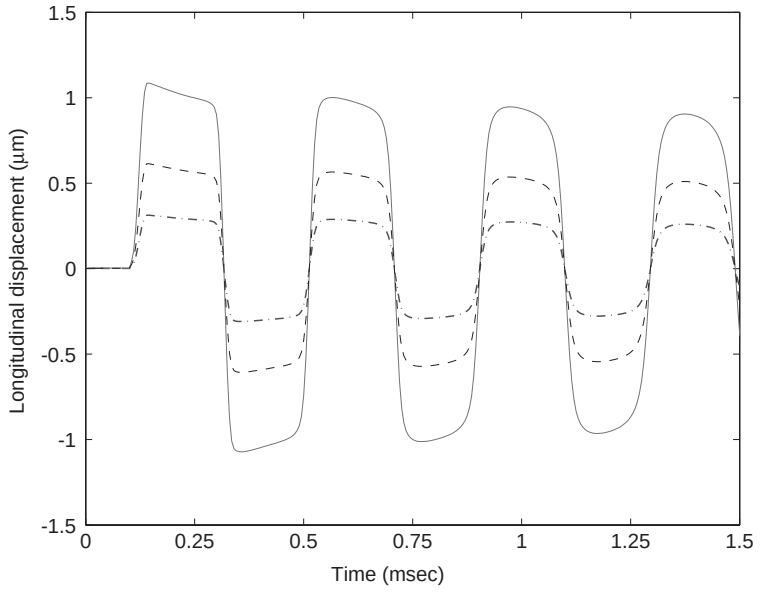

Fig. 13. Longitudinal displacement history $u(t)$ at a point on the outer top-surface ($y = 0, z = R + h$) at the free end ($x = 1$ m) of the clamped–free composite tube for different fiber angles: -.-.-, $\theta = [0^\circ]_{20}$; ——, $\theta = [+45^\circ]_{10}/[-45^\circ]_{10}$; - - -, $\theta = [0^\circ]_{10}/[90^\circ]_{10}$.

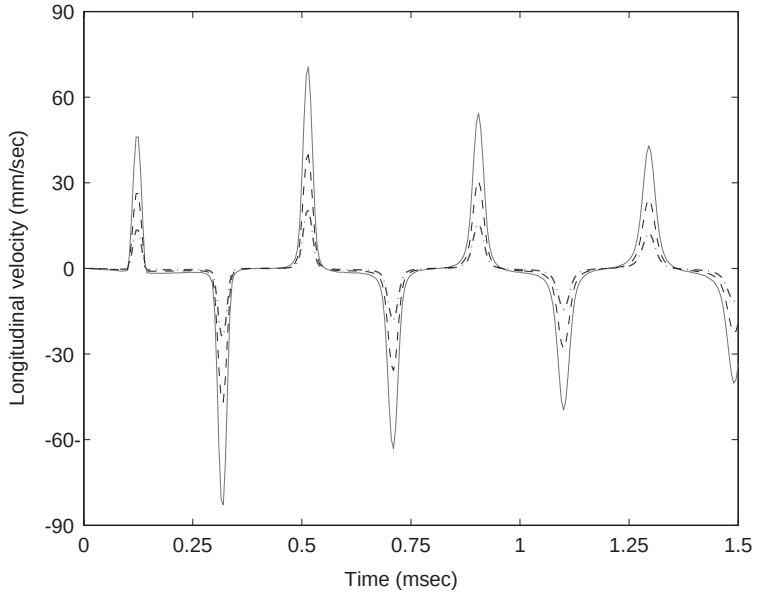

Fig. 14. Longitudinal velocity history $\dot{u}(t)$ at a point on the outer top-surface ($y = 0, z = R + h$) at the free end ($x = 1$ m) of the clamped–free composite tube for different fiber angles: -.-.-, $\theta = [0^\circ]_{20}$; ——, $\theta = [+45^\circ]_{10}/[-45^\circ]_{10}$; - - -, $\theta = [0^\circ]_{10}/[90^\circ]_{10}$.

For load applied in Z-direction, the deformed outer surface ($\xi = h$) geometry is snapped at $t = 0.5$ ms in Fig. 15. The effect of ovaling near the mid-length of the tube can be observed. For three different sets of fiber angle, the transverse displacement and the transverse velocity histories at the point $(1, 0, R + h)$ on the free end are shown, respectively, in Figs. 16 and 17. Unlike axial

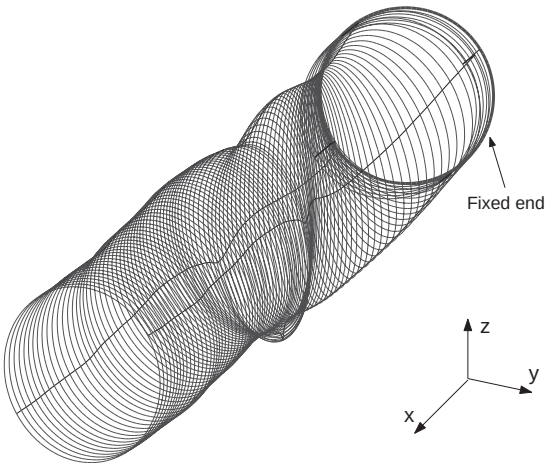

Fig. 15. Snap of outer surface geometry at $t = 0.5$ ms for the graphite–epoxy composite clamped–free tube ($L = 1$ m, $L/R = 50$, $\eta = 0.1$ with $\theta = 0^\circ$ lay-up). A short-pulse load (Fig. 9) is applied uniformly at the free end along the Z-direction. Scale-factor for displacement amplification is 1×10^7.

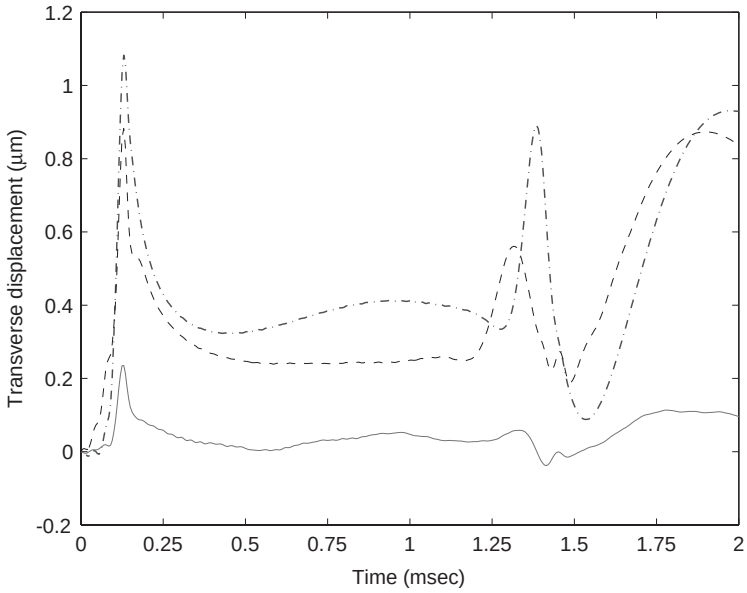

Fig. 16. Transverse displacement history $w(t)$ at a point on the outer top-surface ($y = 0$, $z = R + h$) at the free end ($x = 1$ m) of the clamped–free composite tube for different fiber angles: -.-.-, $\theta = [0^\circ]_{20}$; ——, $\theta = [+45^\circ]_{10}/[-45^\circ]_{10}$; - - - $\theta = [0^\circ]_{10}/[90^\circ]_{10}$.

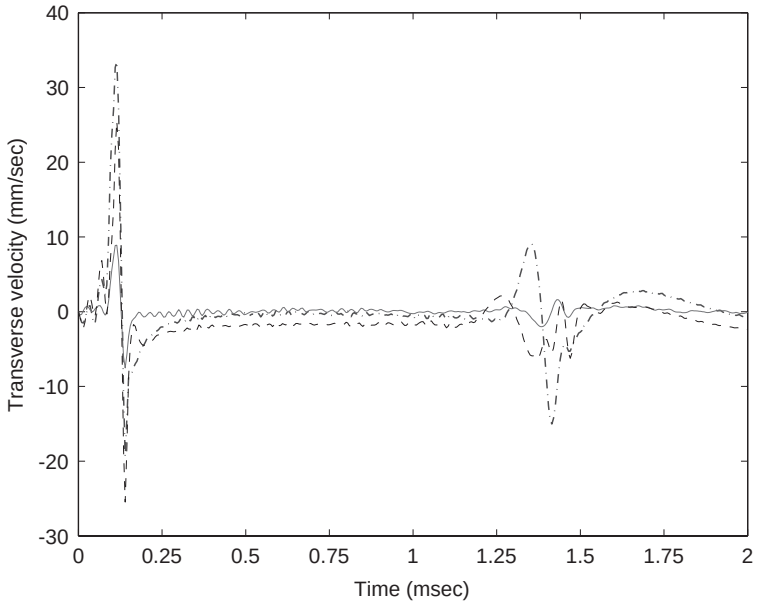

Fig. 17. Transverse velocity history $\dot{w}(t)$ at a point on the outer top-surface ($y = 0$, $z = R + h$) at the free end ($x = 1$ m) of the clamped–free composite tube for different fiber angles: -.-.-, $\theta = [0^\circ]_{20}$; ——, $\theta = [+45^\circ]_{10}/[-45^\circ]_{10}$; - - -, $\theta = [0^\circ]_{10}/[90^\circ]_{10}$.

responses shown earlier, here, the responses are dispersive. After the initial incidence of the impact, one reflection from the clamped end of the tube can be seen in both the responses which arrive at the measurement point at about $t = 1.4$ ms. As compared to the axial response, here the $\theta = [0^\circ]_{20}$ configuration generates maximum transverse response. There are small distortions in the predicted responses before the incidence of impact (before $t = 50$ μs), which is due to frequency window wrap-around during inverse FFT and is inherent to any analysis in transformed finite domain.

For torsional load applied about X-axis, the deformed outer surface ($\xi = h$) geometry is snapped at $t = 0.5$ ms in Fig. 18. It can be seen that the rings through which the torsional waves have propagated towards the clamped end have bulged almost axisymmetrically which can be attributed to the combined effect of antisymmetric thickness stretching and rotational inertia of the tube cross-section. For three different sets of fiber angle, lateral displacement and lateral velocity histories at the point $(1, 0, R + h)$ on the free end are shown, respectively, in Figs. 19 and 20. Although the torsional waves are non-dispersive for $\theta = 0^\circ$ (see the dispersion curve in Fig. 2), the lateral flexural waves are dispersive and finally the combined effect (Eq. (2)) in the lateral motion on outer top surface becomes attenuating in nature. Due to this reason, incident peaks and reflected peaks can be visible only in velocity history (Fig. 20) that has dimensional similarity with phase velocity of the dispersive waves. The displacement and velocity histories corresponding to $\theta = [+45^\circ]_{10}/[-45^\circ]_{10}$ configuration are, respectively, 2 and 3 order smaller compared to those from other two configurations. As in the plots of transverse responses against transverse loading,

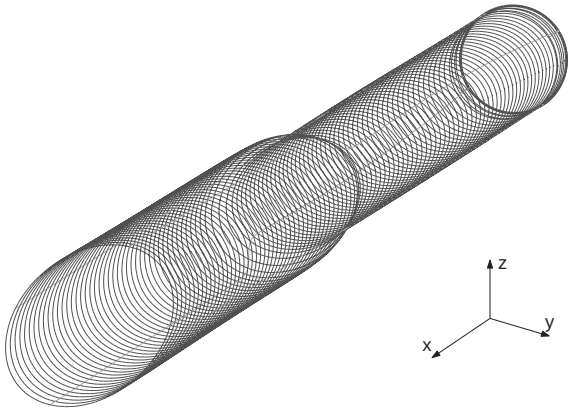

Fig. 18. Snap of outer surface geometry at $t = 0.5$ ms for the graphite–epoxy composite clamped–free tube ($L = 1$ m, $L/R = 50$, $\eta = 0.1$ with $\theta = 0^\circ$ lay-up). A short-pulsed torsional loading of peak amplitude 100 N m (similar to Fig. 9) is applied uniformly at the free end about X-axis. Scale-factor for displacement amplification is 1×10^6.

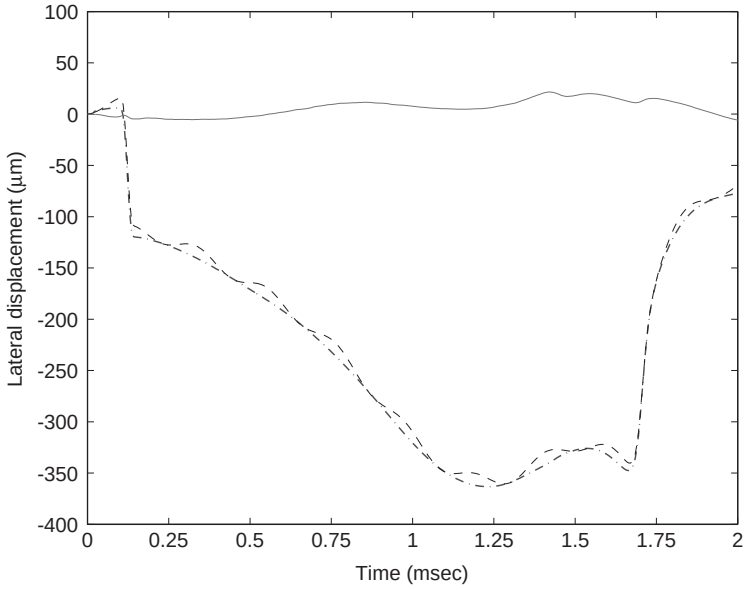

Fig. 19. Lateral displacement history $v(t)$ at a point on the top surface ($y = 0$, $z = R + h$) at the free end ($x = 1$ m) of the clamped–free composite tube for different fiber angles: -.-.-, $\theta = [0^\circ]_{20}$; ——, $\theta = [+45^\circ]_{10}/[-45^\circ]_{10}$; - - -, $\theta = [0^\circ]_{10}/[90^\circ]_{10}$.

here also small errors due to window distortion in the initial responses (before $t = 50$ μs) have occurred. However, these errors are within acceptable range and does not alter the nature of response. Also, these errors can be eliminated by expanding the length of the frequency window with appropriate resolution.

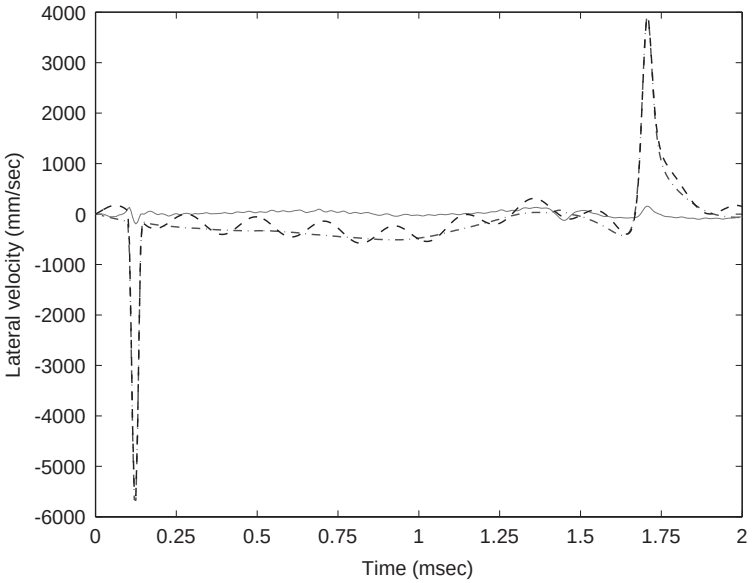

Fig. 20. Lateral velocity history $\dot{v}(t)$ at a point on the outer top surface ($y = 0$, $z = R + h$) at the free end ($x = 1$ m) of the clamped–free composite tube for different fiber angles: -.-.-, $\theta = [0^\circ]_{20}$; ——, $\theta = [+45^\circ]_{10}/[-45^\circ]_{10}$; - - -, $\theta = [0^\circ]_{10}/[90^\circ]_{10}$.

4.3. Parametric study of impact-induced response

Here we present two parametric studies on a clamped–free graphite–epoxy composite tube, as considered earlier, with varying geometry and varying fiber angle. The objective is to obtained the nature of variation of the maximum response due to incident impact at the free-end node for different L/R and η. For this purpose, the measure for a particular fiber angle θ is chosen as maximum displacement normalized with respect to maximum displacement for $\theta = 0$. Here all the layers are considered to have same θ. In the first type of parametric variation, $\eta = 0.1$ is fixed and L/R is varied from 20 to 100. For each of these geometries, normalized maximum displacements are computed for $\theta = 0$–90° in steps of 10°. In the second type of parametric variation, $L/R = 50$ is fixed and η is varied from 0.25 to 0.05. For each of these geometries, normalized maximum displacements are computed for $\theta = 0^\circ$–90° in steps of 10°. The plots are shown in Figs. 21–26.

From plots of $\log_{10}[u^o_{max}/u^o_{max}\ (\theta = 0^\circ)]$ in Figs. 21 and 22, it can be seen that maximum axial displacement occurs for $\theta = 30^\circ$ irrespective of the geometry. At this fiber angle, amplitude level first increases for increasing L/R up to 60 and again decreases towards $L/R = 100$. From plots of $\log_{10}[w^o_{max}/w^o_{max}\ (\theta = 0^\circ)]$ in Figs. 23 and 24, it can be observed that maximum displacements occur at $\theta = 10^\circ$ irrespective of geometry. Although, relative change in amplitude level when compared to $\theta = 0^\circ$ for individual cases vary arbitrarily at different θ, one order difference can be found when compared to those for axial motion in Figs. 21–26. From plots of $\log_{10}[\theta^o_{x\,max}/\theta^o_{x\,max}\ (\theta = 0^\circ)]$ in Figs. 25 and 26, it can be seen that the behavior for varying L/R as well as varying η is similar to those in axial motion and relative change in the amplitude level

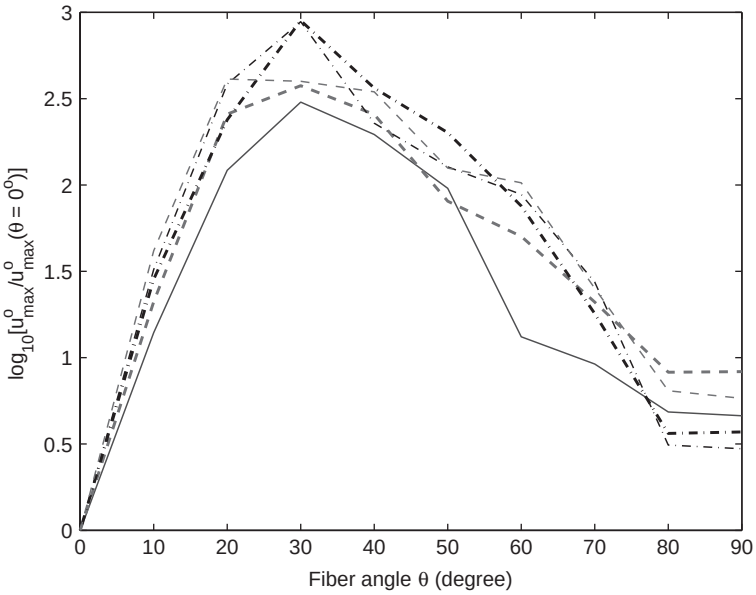

Fig. 21. Plot of $\log_{10}[u^o_{max}/u^o_{max}(\theta = 0^\circ)]$ at the free-end cross-section of the clamped–free composite tube for various L/R and various fiber angles θ, $\eta = 0.1$: ——, $L/R = 20$; - - -, $L/R = 40$; -.-.-, $L/R = 60$; -.-.-, $L/R = 80$; - - -, $L/R = 100$.

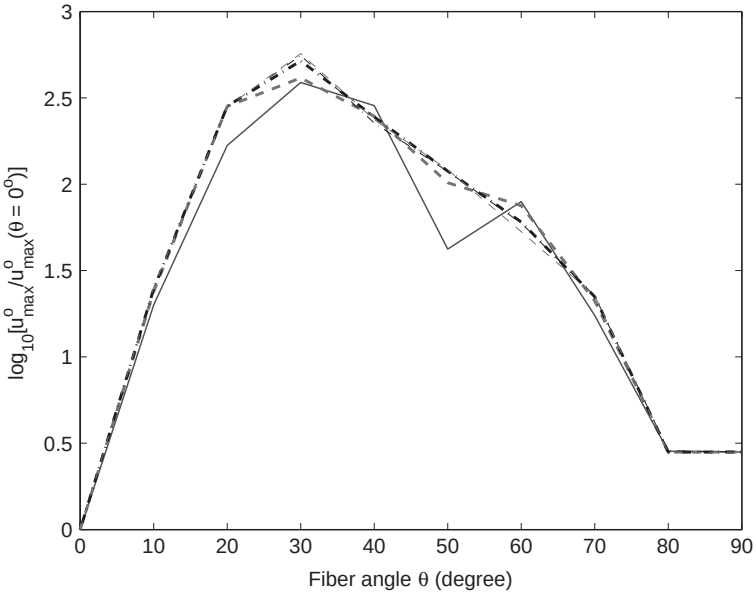

Fig. 22. Plot of $\log_{10}[u^o_{max}/u^o_{max}(\theta = 0^\circ)]$ at the free-end cross-section of the clamped–free composite tube for various R/t and various fiber angle θ, $L/R = 50$: ——, $\eta = 0.25$; - - -, $\eta = 0.125$; -.-.-, $\eta = 0.0833$; -.-.-, $\eta = 0.0625$; - - -, $\eta = 0.05$.

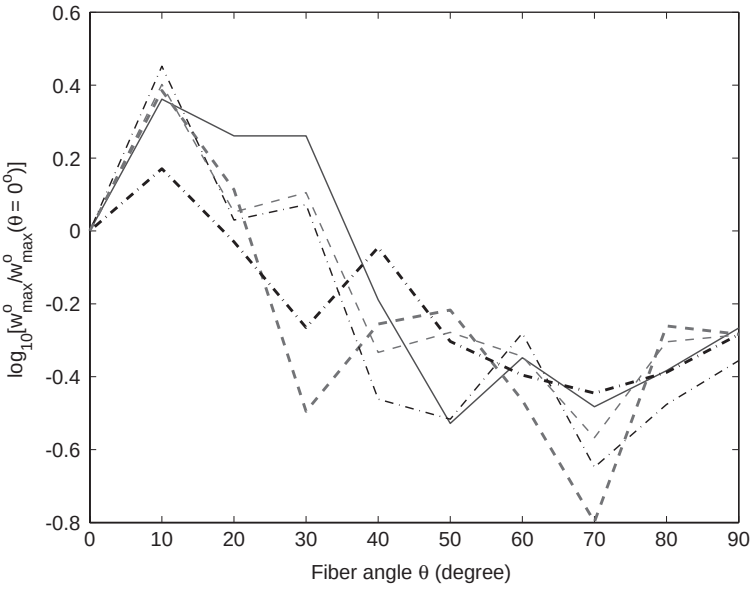

Fig. 23. Plot of $\log_{10}[w^o_{max}/w^o_{max}(\theta = 0^\circ)]$ at the free end cross-section of the clamped–free composite tube for various L/R and various fiber angle θ, $\eta = 0.1$: ——, $L/R = 20$; - - -, $L/R = 40$; -.-.-, $L/R = 60$; -.-.-, $L/R = 80$; - - -, $L/R = 100$.

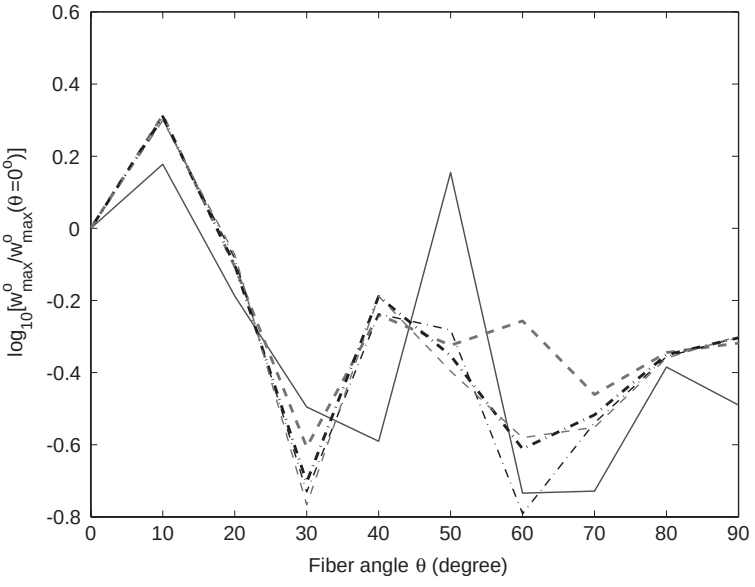

Fig. 24. Plot of $\log_{10}[w^o_{max}/w^o_{max}(\theta = 0^\circ)]$ at the free-end cross-section of the clamped–free composite tube for various R/t and various fiber angle θ, $L/R = 50$: ——, $\eta = 0.25$; - - -, $\eta = 0.125$; -.-.-, $\eta = 0.0833$; -.-.-, $\eta = 0.0625$; - - -, $\eta = 0.05$.

with respect to $\theta = 0^\circ$ is also similar. Maximum rotation of the tube cross-section occurs near $\theta = 30^\circ$ irrespective of the geometry. Also, it can be observed in Fig. 26 that the effect of variation of η below $\theta = 10^\circ$ and above $\theta = 40^\circ$ is insignificant.

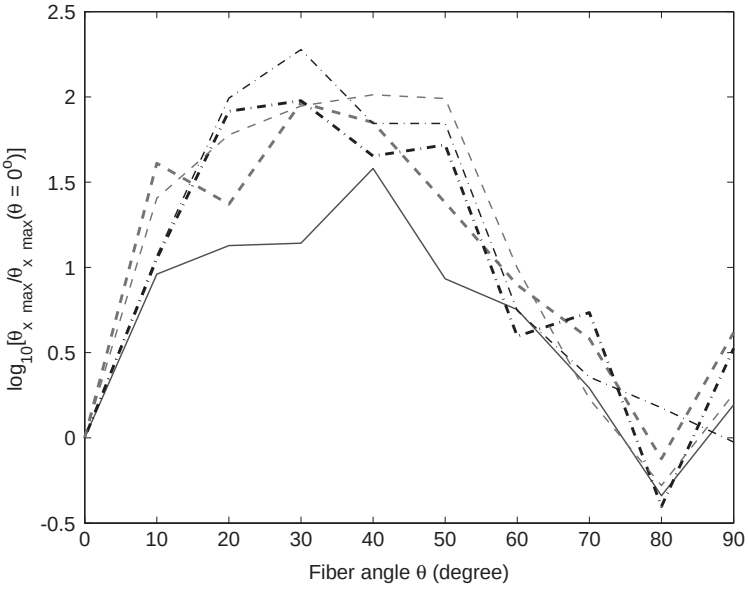

Fig. 25. Plot of $\log_{10}[\theta^o_{x\,max}/\theta^o_{x\,max}(\theta = 0^\circ)]$ at the free-end cross-section of the clamped–free composite tube for various L/R and various fiber angle θ, $\eta = 0.1$: ——, $L/R = 20$; - - -, $L/R = 40$; -.-.-, $L/R = 60$; -.-.-, $L/R = 80$; - - -, $L/R = 100$.

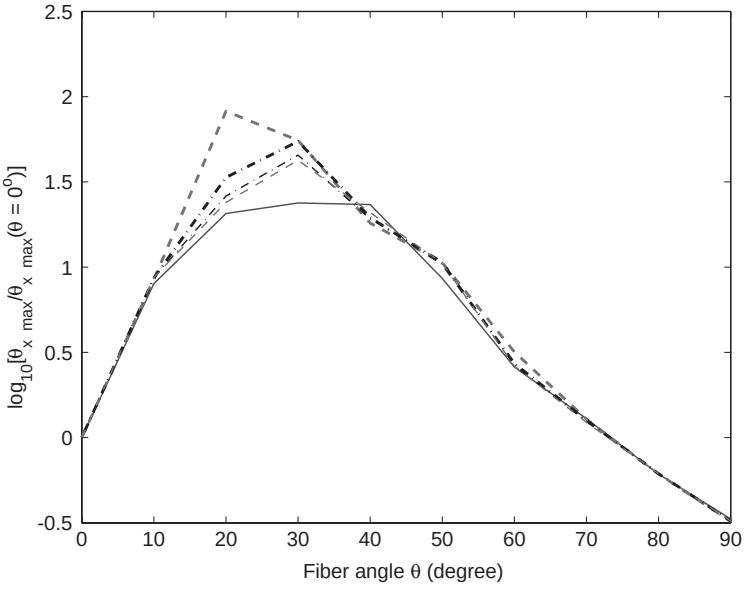

Fig. 26. Plot of $\log_{10}[\theta^o_{x\,max}/\theta^o_{x\,max}(\theta = 0^\circ)]$ at the free-end cross-section of the clamped–free composite tube for various R/t and various fiber angle θ, $L/R = 50$: ——, $\eta = 0.25$; - - -, $\eta = 0.125$; -.-.-, $\eta = 0.0833$; -.-.-, $\eta = 0.0625$; - - -, $\eta = 0.05$.

5. Conclusions

A spectral finite element model (SFEM) for analysis of coupled broadband wave propagation in uniform composite tube is presented. Related computational complexities, advantages and limitations of the model for impact induced wave propagation are also discussed. The systematic formulation in wavenumber space integrated with standard FE approach presented here shows the possibility of automated wave propagation analysis in more complex composite cylindrical shells and connected structures. Apart from this main scope of discussions in the paper, numerical simulations using the new element are performed. In this portion of the work, a map of the distribution of vibrational modes and their effect on overall dynamics in wavelength and time scales have been discussed. The approach developed here is for general purpose computational simulation and does not depend on availability of closed-form expressions to obtain mode count. Under impact type loading, various time responses and post-processing capabilities are illustrated. Much higher computational efficiencies compared to standard FE model can be achieved using this SFEM while solving vibration and wave propagation problems in large connected tubular structures. Finally, attempt is made to capture the effects of tube geometry and fiber angle on the impact-induced response of clamped–free graphite–epoxy composite tube. The simulation shows that the cantilever structure under tip impact load has maximum response for fiber angle $\theta = 30^\circ$ for axial and torsional motions and fiber angle $\theta = 10^\circ$ for transverse motion. More detailed parametric studies on similar aspects along with general higher-order shell kinematics can provide important inputs for improved design of such slender composite tubes operating in transient dynamic environment.

Appendix

$$(\mathbf{A}_{jl}, \mathbf{M}) = \int_0^{2\pi} \int_{R-h}^{R+h} (\bar{\bar{Q}}_{jl}, \rho) \times \begin{bmatrix} 1 & y & z & \bar{y} & \bar{z} & \bar{y},_y & \bar{y},_z & \bar{z},_y & \bar{z},_z \\ & y^2 & yz & y\bar{y} & y\bar{z} & y\bar{y},_y & y\bar{y},_z & y\bar{z},_y & y\bar{z},_z \\ & & z^2 & z\bar{y} & z\bar{z} & z\bar{y},_y & z\bar{y},_z & z\bar{z},_y & z\bar{z},_z \\ & & & \bar{y}^2 & \bar{y}\bar{z} & \bar{y}\bar{y},_y & \bar{y}\bar{y},_z & \bar{y}\bar{z},_y & \bar{y}\bar{z},_z \\ & & & & \bar{z}^2 & \bar{z}\bar{y},_y & \bar{z}\bar{y},_z & \bar{z}\bar{z},_y & \bar{z}\bar{z},_z \\ & & & sym & & \bar{y},_y^2 & \bar{y},_y \bar{y},_z & \bar{y},_y \bar{z},_y & \bar{y},_y \bar{z},_z \\ & & & & & & \bar{y},_z^2 & \bar{y},_z \bar{z},_y & \bar{y},_z \bar{z},_z \\ & & & & & & & \bar{z},_y^2 & \bar{z},_y \bar{z},_z \\ & & & & & & & & \bar{z},_z^2 \end{bmatrix} r \, \mathrm{d}r \, \mathrm{d}\phi,$$

where

$$\bar{\bar{Q}}_{11} = \bar{Q}_{11}, \quad \bar{\bar{Q}}_{15} = \bar{Q}_{16} \cos\phi, \quad \bar{\bar{Q}}_{16} = \bar{Q}_{16} \sin\phi,$$

$$\bar{\bar{Q}}_{55} = \bar{Q}_{55}\sin^2\phi + \bar{Q}_{66}\cos^2\phi, \quad \bar{\bar{Q}}_{56} = (\bar{Q}_{55} - \bar{Q}_{66})\sin\phi\cos\phi,$$

$$\bar{\bar{Q}}_{66} = \bar{Q}_{66}\sin^2\phi + \bar{Q}_{55}\cos^2\phi.$$

References

[1] W.H. Prosser, M.R. Gorman, J. Dorighi, Extensional and flexural waves in a thin-walled graphite/epoxy tube, Journal of Composite Materials 26 (14) (1992) 418–427.
[2] W.B. Fitchter, A theory for inflated thin-wall cylindrical beams, NASA Technical Note TN D-3466, 1966.
[3] S. Gopalakrishnan, D. Roy Mahapatra, Active control of structure-borne noise in helicopter cabin transmitted through gearbox support strut, in: M.L. Munjal (Ed.), Proceedings of IUTAM Symposium on Designing for Quietness, Solid Mechanics and its Applications, Vol. 102, Kluwer Academic Publishers, Dordrecht, 2002.
[4] I. Mirsky, G. Herrmann, Nonaxially symmetric motions of cylindrical shells, Journal of the Acoustical Society of America 29 (1957) 1116–1123.
[5] R.M. Cooper, P.M. Naghdi, Propagation of nonaxially symmetric waves in elastic cylindrical shells, Journal of the Acoustical Society of America 29 (1957) 1365–1372.
[6] J.E. Greenspon, Vibration of a thick-walled cylindrical shell—comparison of the exact theory with the approximate theories, Journal of the Acoustical Society of America 32 (1960) 571–578.
[7] J.N. Reddy, C.F. Liu, A higher-order shear deformation theory of laminated elastic shells, International Journal of Engineering Science 23 (1985) 440–447.
[8] A.W. Leissa, J. Chang, Elastic deformation of thick, laminated composite shallow shells, Composite Structures 35 (1996) 153–170.
[9] M.S. Qatu, Accurate equations for laminated composite deep thick shells, International Journal of Solids and Structures 36 (1999) 1917–2941.
[10] D.C. Gazis, Three dimensional investigation of the propagation of waves in hollow circular cylinders—I. Analytical foundation II. Numerical results, Journal of the Acoustical Society of America 31 (1959) 568–578.
[11] Z.C. Xi, G.R. Liu, K.Y. Lam, H.M. Shang, Dispersion and characteristic surfaces of waves in laminated composite circular cylindrical shells, Journal of the Acoustical Society of America 108 (5) (2000) 2179–2186.
[12] G. Sun, P.N. Bennett, F.W. Williams, An investigation on fundamental frequencies of laminated circular cylinders given by shear deformable finite element, Journal of Sound and Vibration 205 (3) (1997) 265–273.
[13] J.N. Reddy, Bending of laminated anisotropic shells by a shear deformable finite element, Composite Science and Technology 17 (1982) 9–24.
[14] J.N. Reddy, Exact solutions pf moderately thick shells, Journal of Engineering Mechanics Division, American Society of Civil Engineers 110 (1984) 794–809.
[15] K. Chandrashekhara, Free vibrations of anisotropic laminated doubly curved shells, Computers and Structures 33 (1989) 435–440.
[16] R.S. Langley, Wave motion and energy flow in cylindrical shells, Journal of Sound and Vibration 169 (1) (1994) 29–42.
[17] R.S. Langley, The modal density and mode count of thin cylindrical and curved panels, Journal of Sound and Vibration 169 (1) (1994) 43–53.
[18] P.W. Smith, Phase velocity and displacement characteristics of free waves in thin cylindrical shells, Journal of the Acoustical Society of America 27 (1955) 1065–1072.
[19] C.R. Fuller, F.J. Fahy, Characteristics of wave propagation and energy distribution in cylindrical elastic shells filled with fluid, Journal of Sound and Vibration 81 (1981) 501–518.
[20] Z.C. Xi, G.R. Liu, K.Y. Lam, S.M. Shang, A strip element method for analyzing wave scattering by a crack in a fluid-filled composite cylindrical shell, Composite Science and Technology 60 (2000) 1985–1996.
[21] M. Ruzzene, A. Baz, Active control of wave propagation in periodic fluid-loaded shells, Smart Materials and Structures 10 (2001) 893–906.

[22] X. Han, G.R. Liu, Z.C. Xi, K.Y. Lam, Transient waves in a functionally graded cylinder, International Journal of Solids and Structures 38 (2001) 3021–3037.
[23] X. Han, G.R. Liu, Z.C. Xi, K.Y. Lam, Characteristics of waves in a functionally graded cylinder, International Journal of Numerical Methods in Engineering 53 (2002) 653–676.
[24] M.S. Bennett, M.L. Accorsi, Free wave propagation in periodically ring stiffened cylindrical shells, Journal of Sound and Vibration 171 (1) (1994) 49–66.
[25] J.D. Kaplunov, L.Yu. Kossovich, E.V. Nolde, Dynamics of Thin Walled Elastic Bodies, Academic Press, London, 1998.
[26] O. Song, L. Liberescu, Structural modeling and free vibration analysis of rotating composite thin-walled beams, Journal of the American Helicopter Society, Oct (1997) 358–369.
[27] O. Rand, Fundamental closed-form solutions for solid and thin-walled composite beams including a complete out-of-plane warping model, International Journal of Solids and Structures 35 (21) (1998) 2775–2793.
[28] E.A. Armanios, A.M. Badir, Free vibration analysis of anisotropic thin-walled closed-section beams, American Institute of Aeronautics and Astronautics Journal 33 (10) (1995) 1905–1910.
[29] D.S. Dancila, E.A Armanios, The influence of coupling on the free vibration of anisotropic thin-walled closed-section beams, International Journal of Solids and Structures 35 (23) (1998) 3105–3119.
[30] J.F. Ferrero, J.J. Barrau, J.M. Segura, B. Castanie, M. Sudre, Torsion of thin-walled composite beams with midplane symmetry, Composite Structures 54 (1) (2001) 111–120.
[31] X. Wang, K. Zhang, W. Zhang, J.B. Chen, Theoretical solution and finite element solution for an orthotropic thick cylindrical shell under impact load, Journal of Sound and Vibration 236 (1) (2000) 129–140.
[32] J.F. Doyle, Wave Propagation in Structures, Springer, NY, 1997.
[33] D. Roy Mahapatra, S. Gopalakrishnan, T.S. Sankar, Spectral-element-based solutions for wave propagation analysis of multiply connected laminated composite beams, Journal of Sound and Vibration 237 (5) (2000) 819–836.
[34] D. Roy Mahapatra, S. Gopalakrishnan, A spectral finite element model for analysis of axial–flexural-shear coupled wave propagation in laminated composite beams, Composite Structures 59 (1) (2003) 67–88.
[35] J.N. Reddy, Mechanics of Laminated Composite Plates, CRC Press, Boca Raton, FL, 1997.
[36] G.R. Cowper, The shear coefficient in Timoshenko's beam theory, Journal of Applied Mechanics 33 (1996) 335–340.
[37] IMSL Mathematics and Statistics Libraries, Visual Numerics, Inc., San Ramon, CA, 2001.
[38] K.F. Graff, Wave Motion in Elastic Solids, Dover, NY, 1975.